nature aging

Article

https://doi.org/10.1038/s43587-024-00694-0

Aged bone marrow macrophages drive systemic aging and age-related dysfunction via extracellular vesicle-mediated induction of paracrine senescence

Received: 2 December 2023

Accepted: 25 July 2024

Published online: 12 September 2024

Check for updates

Jing Hou[1,10], Kai-Xuan Chen[1,10], Chen He[1], Xiao-Xiao Li[2,3], Mei Huang[1], Yang-Zi Jiang[4,5], Yu-Rui Jiao[1], Qiao-Ni Xiao[1], Wen-Zhen He[1], Ling Liu[1], Nan-Yu Zou[1], Min Huang[1], Jie Wei[2,3,6,7], Ye Xiao[1], Mi Yang[1], Xiang-Hang Luo[1,3,8], Chao Zeng[2,3,6,7,8] ✉, Guang-Hua Lei[2,3,6,8] ✉ & Chang-Jun Li[1,3,8,9] ✉

The accumulation and systemic propagation of senescent cells contributes to physiological aging and age-related pathology. However, which cell types are most susceptible to the aged milieu and could be responsible for the propagation of senescence has remained unclear. Here we found that physiologically aged bone marrow monocytes/macrophages (BMMs) propagate senescence to multiple tissues, through extracellular vesicles (EVs), and drive age-associated dysfunction in mice. We identified peroxisome proliferator-activated receptor α (PPARα) as a target of microRNAs within aged BMM-EVs that regulates downstream effects on senescence and age-related dysfunction. Demonstrating therapeutic potential, we report that treatment with the PPARα agonist fenofibrate effectively restores tissue homeostasis in aged mice. Suggesting conservation to humans, in a cohort study of 7,986 participants, we found that fenofibrate use is associated with a reduced risk of age-related chronic disease and higher life expectancy. Together, our findings establish that BMMs can propagate senescence to distant tissues and cause age-related dysfunction, and they provide supportive evidence for fenofibrate to extend healthy lifespan.

Aging stands as the foremost risk factor for a diverse array of chronic diseases in humans, such as diabetes, osteoporosis, sarcopenia, Alzheimer's disease and more[1–6]. One underlying contributor to these age-related disorders is the widespread accumulation of senescent cells within tissues, profoundly disturbing tissue integrity and function[7–11]. Cellular senescence[12–14] is characterized by permanent cell cycle arrest, apoptosis resistance and a complex senescence-associated secretory phenotype (SASP)[2,3,15–17]. Importantly, senescent cells can initiate a secondary senescence response in neighboring non-senescent cells[18–22]. Thus, identifying the cell types responsible for senescence propagation offers attractive targets for delaying aging and combating age-related diseases.

Several cell types have been reported to propagate senescence within bone marrow, including skeletal stem cells[20], bone marrow adipocytes[19] and bone marrow monocytes/macrophages (BMMs)[23]. We recently reported that senescent BMMs induce skeletal aging, manifested by low bone turnover and marrow fat accumulation[23]. Conversely, young bone marrow shows ability to improve cognition[24]

A full list of affiliations appears at the end of the paper. ✉e-mail: zengchao@csu.edu.cn; lei_guanghua@csu.edu.cn; lichangjun@csu.edu.cn

and muscle atrophy[25]. These studies suggest the great potential of bone marrow in contributing to senescence propagation and systemic aging. As one of the body's largest organs, bone marrow plays pivotal roles in hematopoiesis regulation[26], immune function[27,28] and skeletal quality[20,23]. Exploring the contribution of senescent cells within bone marrow to systemic aging in other tissues may yield attractive strategies for slowing down aging.

Extracellular vesicles (EVs) are lipid bilayer membrane-delimited, nanometer-sized to micrometer-sized particles that appear to be released by all cell types, including senescent cells[29–31]. EVs mediate intercellular communications and affect various physiological and pathological conditions in autocrine, paracrine and endocrine fashion[32–35]. Recent studies have shown that EVs play an important role in cellular senescence[36], aging[37] and age-related diseases[38–41]. EVs isolated from primary fibroblasts of young human donors and healthy hypothalamic stem cells were found to ameliorate senescence in vivo and in vitro[39,42]. However, the source of senescence-associated EVs, the role of EVs on senescence transfer and the functional cargos within EVs are poorly understood.

Elimination of senescent cells[8,43,44] has emerged as a plausible therapeutic approach for preventing, delaying or alleviating multiple diseases and age-related dysfunction[3,45–49]. Senolytics, which are drugs designed to selectively target senescent cells[50], show promising results in preclinical models and clinical trials[33,51–53], However, long-term safety and efficacy of senolytics have not been clinically proven. Here we show that senescent BMMs within bone marrow drive systemic aging and age-related dysfunction via EV-loaded microRNAs (miRNAs). Furthermore, we report that fenofibrate (an FDA-approved lipid-lowering drug) can antagonize the pro-aging effects of senescent BMMs, and its use is associated with a lower incidence of age-related chronic conditions in humans. In addition, participants taking fenofibrate consistently showed increased life expectancy. The discovery of fenofibrate's rejuvenating properties may make it an exploitable therapy for alleviating age-related diseases, providing a rapid and cost-saving opportunity for clinical translation.

Results

Aged bone marrow induces aging and age-related disorders

To explore the contribution of aged bone marrow to systemic aging, young (3 months old) recipient mice were irradiated before injection of donor bone marrow cells from either young (3 months old, YBMT) or aged (24 months old, ABMT) mice to achieve nearly complete (>90%) reconstitution with donor bone marrow (Fig. 1a and Extended Data Fig. 1a). Young mice without transplantation were used as control. We found that transplantation of aged bone marrow increased or tended to increase the expression of senescence-upregulated genes *Cdkn2a* and *Cdkn1a* and SASP factors *Il-1β*, *Il-6* and *Mmp13* in multiple tissues, including liver, skeletal muscle and white adipose tissue (Fig. 1b and Extended Data Fig. 1b). The induction of senescence in young tissues by aged bone marrow was also confirmed by increased levels of p53, p21 and γ-H2A.X protein in liver (Fig. 1c), senescence-associated β-galactosidase (SA-β-gal) and γ-H2A.X foci in bone (Fig. 1d and Extended Data Fig. 1c) and p53 and γ-H2A.X foci in brain (Fig. 1d and Extended Data Fig. 1d). Aging is correlated with molecular and functional alterations in various tissues. Young recipients receiving aged bone marrow showed elevated blood glucose levels and inactivation of insulin signaling pathways in liver, muscle and adipose tissue (Fig. 1e,f and Extended Data Fig. 1e–g). We also observed negative effects of aged bone marrow on the skeletal system of young mice, as reflected by lower trabecular bone volume (Fig. 1g and Extended Data Fig. 1h,i). In addition, aged bone marrow resulted in a decrease in the number of neuronal Nissl bodies and the expression of glutamate receptor-1 (GluR-1) in the young brain (Extended Data Fig. 1j–m).

We next asked whether eliminating senescent cells in bone marrow of aged mice with senolytics[54], namely dual treatment with Dasatinib and Quercetin (D+Q), would blunt the propagation of senescence from aged mice to young recipients. We found that D+Q treatment reduced senescent cells in the bone marrow of aged mice (21 months old) (Extended Data Fig. 2a–c). Noticeably, recipients of D+Q-pre-treated aged bone marrow (DQ-ABMT) showed attenuated induction of senescence compared to recipients of vehicle-treated aged bone marrow (ABMT), including attenuated upregulation of the senescence-associated genes *Cdkn2a* and *Cdkn1a* and SASP-related factors *Il-1β*, *Il-6*, *Tnf-α*, *Mmp10* and *Mmp13* in multiple young tissues (Extended Data Fig. 2d–g). In addition, the expression of systemically induced senescence-associated markers, such as SA-β-gal-positive cells in liver, adipose tissue, bone and brain and p21 and γ-H2A.X protein levels in liver, muscle and adipose tissue, showed attenuated upregulation in the DQ-ABMT transplant recipients (Fig. 1h–j and Extended Data Fig. 2d,e,h). Furthermore, the decline of systemic insulin sensitivity and liver steatosis seen in the ABMT group were not observed in the DQ-ABMT group (Fig. 1k,l and Extended Data Fig. 2i–n). Clearance of senescent cells also abolished the negative effects of aged bone marrow on the function and structure of skeleton, muscle and brain (Fig. 1m–o and Extended Data Fig. 2o–q). Together, these findings establish that the senescent phenotype can be propagated from aged mice to young mice via bone marrow.

Macrophages are a major cell type for propagating senescence

To explore which component of the bone marrow is the major driver of aging, we performed a bioinformatics analysis using a single-cell RNA sequencing (scRNA-seq) dataset of bone marrow from young mice (2 months old) and old mice (23 months old)[55]. We found that more than 80% of bone marrow cells were immune cells, and, among them, the number and proportion of monocytes/macrophages and neutrophils in the total bone marrow cells increased considerably with age by cell

Fig. 1 | Aged bone marrow causes senescence propagation in multiple young organs. a, Experimental setup for bone marrow transplantation. Young recipients (3 months old, male mice) were lethally irradiated and then transplanted with bone marrow from young donors (3 months old, male mice) and aged donors (24 months old, male mice). **b**, The mRNA levels of senescence-associated genes and SASP factors in liver, muscle and adipose tissue of young recipients receiving bone marrow transplantation (YBMT and ABMT) ($n = 4$ mice for ABMT; $n = 3$ mice for other groups). **c**, Western blot analysis of p53, p21 and γH2A.X protein expression in liver (left) and quantitative analysis (right) ($n = 3$ mice). **d**, Immunofluorescence detection of γH2A.X in femur and brain (scale bar, 50 μm; $n = 5$ mice) (left) and quantitative analysis (right). **e**, GTT and ITT ($n = 5$ mice). **f**, Western blot analysis of phosphorylated key molecules of insulin pathway in the liver (left) and quantitative data (right) ($n = 3$ mice). **g**, Representative μCT images of recipient mice after transplantation (left) and quantitative analysis of trabecular bone volume/tissue volume (BV/TV) (right) ($n = 5$ mice). **h**, Old mice (16 months old, male) were treated with vehicle or D+Q for 5 months. After 5 months, bone marrow was isolated from mice and transplanted into young mice (3 months old, male) (ABMT and DQ-ABMT). Western blot analysis of p21 and γH2A.X protein expression in liver ($n = 4$ mice for ABMT; $n = 3$ mice for other groups) and adipose tissue ($n = 6$ mice for ABMT; $n = 5$ mice for other groups) (left) of young recipients receiving bone marrow from DQ-treated aged mice, and quantitative analysis (right). **i**,**j**, Representative images of SA-β-gal staining in the adipose tissue (**i**) and femur (**j**) (scale bar, 50 μm; $n = 5$ mice) (left), and their quantitative analysis (right). The red arrows represent the SA-β-gal-positive cells. **k**,**l**, GTT (**k**) and ITT (**l**) were performed on young recipients after transplantation ($n = 6$ mice). **m**, Representative μCT images (left) and quantitative analysis (right) ($n = 6$ mice). The colored shading in **e**, **k** and **l** represents the area under the curve. **n**, Hanging endurance ($n = 6$ mice). **o**, Novel object recognition ($n = 6$ mice). Data are presented as mean ± s.e.m. $^*P < 0.05$, $^{**}P < 0.01$ and $^{***}P < 0.001$, as determined by one-way ANOVA followed by Tukey's multiple comparison test. BM, bone marrow; FDR, false discovery rate; I.V., intravenous; mo, months; Rel. fold, relative fold; T.Ar, total area.

https://doi.org/10.1038/s43587-024-00694-0

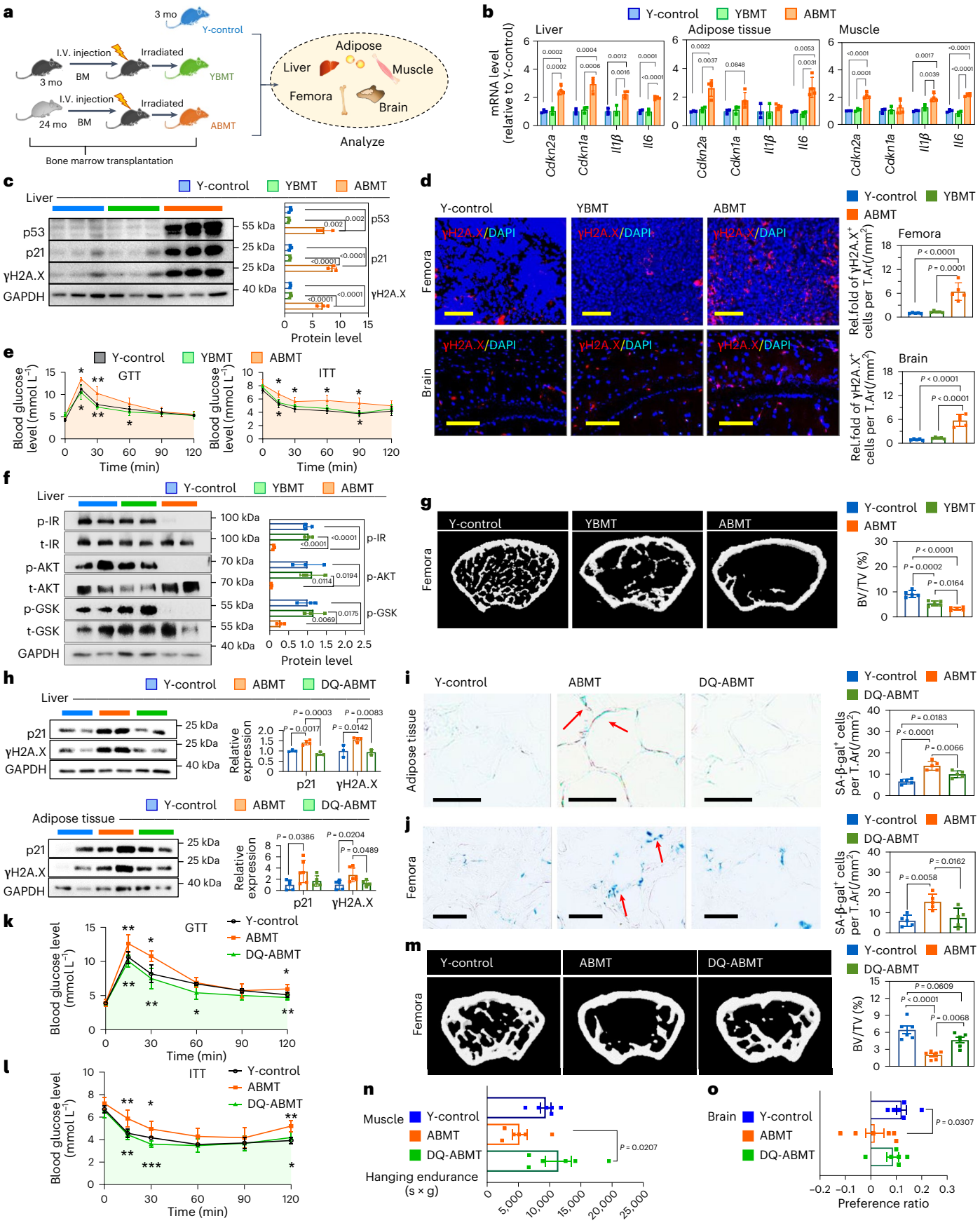

https://doi.org/10.1038/s43587-024-00694-0

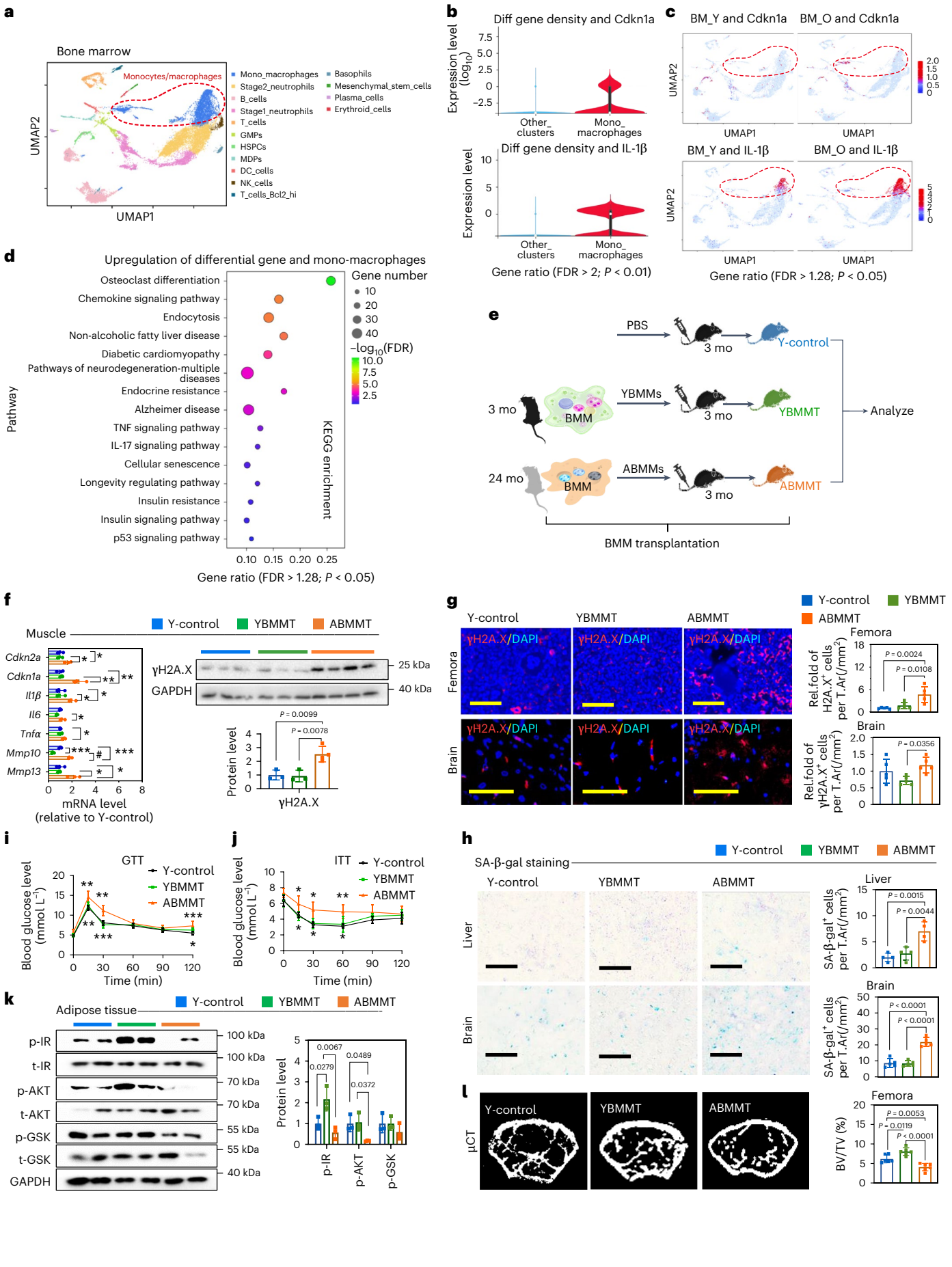

Fig. 2 | Macrophages within bone marrow are the major contributor to aging. **a**, Bioinformatics analysis of scRNA-seq of bone marrow cells from isochronic parabiotic pairs of young mice (2 months old, BM-Y) and old mice (23 months old, BM-O), respectively. **b**, Violin plots show the expression levels of *Cdkn1a* and *Il-β* in the BMMs compared to other cell types. **c**, UMAP plots show the distribution of senescence-related genes in different cell types in young and old bone marrow (BM-Y and BM-O). The red dashed outlines represent the population of monocytes/macrophages. Color bars are the distribution of senescence-related differential genes. **d**, Bubble plot shows the KEGG enrichment pathways for the upregulated aging-related genes in the BMM population. **e**, BMMs were isolated from young mice (3 months old, male, YBMMs) and aged mice (24 months old, male, ABMMs) and then transplanted into young recipients (3 months old, male mice). **f**, Gene expression (left) ($n = 3$ mice) and protein levels (right) ($n = 4$ mice for ABMMT; $n = 3$ mice for other groups) of senescence-associated markers in muscle of young mice transplanted with BMMs (YBMMT and ABMMT). **g**, Immunofluorescence for γH2A.X protein in the femur (upper left) and brain (bottom left) (scale bar, 50 μm; $n = 5$ mice; 5–6 images per mouse), and their quantitative analysis (right). **h**, Representative images of SA-β-gal staining in the liver (scale bar, 50 μm; $n = 4$ mice; 5–6 images per mouse) (upper left) and brain (scale bar, 50 μm; $n = 5$ mice; 5–6 images per mouse) (bottom left), and their quantitative analysis (right). **i**,**j**, GTT (**i**) and ITT (**j**) were performed on young mice transplanted with BMMs ($n = 6$ mice). **k**, Western blot analysis of key molecules of insulin signaling pathway in adipose tissue (left) and quantitative analysis (right) ($n = 3$ mice). **l**, Representative μCT images (left) and quantitative analysis (right) of trabecular bone-related parameters (bone volume/tissue volume (BV/TV)) ($n = 6$ mice). Data are expressed as mean ± s.e.m. for all panels. $^{*}P < 0.05$, $^{**}P < 0.01$, $^{***}P < 0.001$ and $^{\#}P < 0.0001$, as determined by one-way ANOVA followed by Tukey's multiple comparison test. UMAP, uniform manifold approximation and projection. FDR, false discovery rate; mo, months; Diff, differential; Rel. fold, relative fold; T.Ar, total area.

frequency analysis (Fig. 2a and Extended Data Fig. 3a–c). Strikingly, upregulated senescence-related genes and inflammation-related genes were all preferentially enriched in BMMs, including *Cdkn1a*, *Cdkn2a*, *Il-1β*, *Il-18*, *Tnf-α* and *Ccl2*, compared to neutrophils and other cell types (Fig. 2b,c and Extended Data Fig. 3d,e). In addition, Kyoto Encyclopedia of Genes and Genomes (KEGG) analysis showed that the upregulated aging-related differential gene expression profiles in the BMM population were enriched in pathways for regulation of endocrine and metabolic diseases, neurodegenerative diseases and cellular senescence (Fig. 2d). Based on these findings and our recent study showing that senescent BMMs induce bone aging[23], we speculate that, among bone marrow cells, BMMs are more susceptible to the aged milieu and could have a prominent contribution to the physiological process of aging.

Next, we performed transplantation of BMMs from aged mice (aged BMMs) to young mice and found that a high proportion of BMMs isolated from aged mice exhibited phenotypes of senescence (Extended Data Fig. 3f–h). Substantially increased expression of senescence-related factors was observed in liver, muscle, adipose tissue and brain of young mice exposed to aged BMMs (Fig. 2e,f and Extended Data Fig. 3i–k). Furthermore, we established the effects of aged BMMs on propagating senescence by monitoring other senescence markers, such as SA-β-gal-positive cells in liver and brain, γ-H2A.X foci in bone and brain and p21 foci in bone of young recipients (Fig. 2g,h and Extended Data Fig. 3l). Notably, transplantation of aged BMMs to young mice led to age-related dysfunction, including systemic insulin resistance (Fig. 2i–k and Extended Data Fig. 4a–c) and bone mass loss (Fig. 2l and Extended Data Fig. 4d). In addition, we found that aged BMMs also increased synapse engulfment in microglia and decreased expression of GluR-1, indicating that aged BMMs may contribute to cognitive decline (Extended Data Fig. 4e). These findings suggest that BMMs are likely a major bone marrow cell type that propagate systemic senescence during aging.

Aged BMMs drive senescence propagation to young tissues

To further verify the role of senescent BMMs in propagating senescence, BMMs were isolated from aged mice (24 months old) and then pre-treated with senolytics (D+Q) to eliminate senescent BMMs and subsequently transplanted into young recipients (DQ-ABMMT). Vehicle-treated BMMs served as control (ABMMT) (Fig. 3a). As expected, we found that D+Q treatment reduced the proportion of aged BMMs exhibiting the DNA damage marker γ-H2A.X, suggesting a reduction in senescent BMMs (Extended Data Fig. 5a–d). Notably, eliminating senescent BMMs abrogated their intrinsic effects on promoting senescence propagation, as illustrated by the attenuated transcriptional upregulation of *Cdkn1a* and *Cdkn2a* as well as several SASP components (*Il-1β*, *Il-6*, *Tnf-α*, *Cxcl1*, *Mmp10* and *Mmp13*) in multiple tissues of young recipients after transplantation (Fig. 3b and Extended Data Fig. 5e). Moreover, the protein levels of senescence markers and SA-β-gal-positive cells were attenuated in multiple young tissues in the DQ-ABMMT group compared to the ABMMT group (Fig. 3b,c). Noticeably, the DQ-ABMMT group showed improved blood glucose levels (Fig. 3d,e and Extended Data Fig. 5f), hepatic functions (Fig. 3f,g and Extended Data Fig. 5g), insulin sensitivity (Fig. 3h and Extended Data Fig. 5h) and bone mass (Fig. 3i–j) as well as partially improved physical endurance (hanging endurance) (Fig. 3k) and cognitive function (novel object recognition assay) (Fig. 3l and Extended Data Fig. 5i). These results indicate that senescent BMMs induce systemic senescence and age-related dysfunction.

EVs secreted by aged BMMs propagate senescence and aging

Senescence-associated EVs show the potential of mediating cellular senescence[32,56]. To explore whether senescent BMMs propagate senescence to other tissues via EVs, BMM-EVs from young mice (3 months old, YBMM-EVs) or aged mice (20 months old, ABMM-EVs) were collected and transplanted into young recipients (3 months old, male) (Fig. 4a and Extended Data Fig. 6a,b). Strikingly, ABMM-EVs induced the senescence load across multiple young tissues, including liver, muscle, adipose tissue and bone, compared to YBMM-EV treatment (Fig. 4b and Extended Data Fig. 6c–f). In terms of function and metabolism, there were negative effects of ABMM-EVs on glucolipid metabolism in young recipients, as demonstrated by higher blood glucose levels (Fig. 4c and Extended Data Fig. 6g,h), increased hepatic steatosis (Extended Data Fig. 6h–j) and reduced insulin sensitivity (Fig. 4d and Extended Data Fig. 6k). In the skeletal system,

Fig. 3 | Senescent BMMs drive senescence propagation to multiple tissues. **a**, Outline of the studies. BMMs were isolated from aged mice (24 months old, male) and then treated with vehicle or D+Q (ABMM, DQ-ABMM). We subsequently transplanted them into young recipients (3 months old, male mice). **b**, Gene expression (left) ($n = 4$ mice) and protein levels (right) of senescence-associated markers in liver (upper), muscle (middle) and adipose tissue (bottom) of young mice transplanted with DQ-treated BMMs ($n = 5$ mice for ABMMT; $n = 3$ mice for other groups in liver; $n = 3$ mice in muscle and adipose). **c**, Representative SA-β-gal staining in liver (scale bar, 50 μm; $n = 4$ mice; 5–6 images per mouse) (top) and brain (scale bar, 50 μm; $n = 5$ mice; 5–6 images per mouse) (bottom). The red arrows represent the SA-β-gal-positive cells. **d**, GTT and ITT ($n = 6$ mice). **e**, Gene expression of G6Pase, PEPCK and PGC-1α in liver ($n = 4$ mice). **f**, The ratio of liver weight to body weight (LW/BW) ($n = 6$ mice). **g**, The mRNA level of FASN in liver ($n = 4$ mice). **h**, Phosphorylation levels of insulin signaling in liver ($n = 3$ mice for Y-control, $n = 4$ mice for other groups), muscle and adipose tissue ($n = 3$ mice). **i**,**j**, Representative μCT images (**i**) and quantitative analysis of trabecular bone volume/tissue volume (BV/TV) (**j**) ($n = 6$ mice). **k**, Hanging endurance ($n = 6$ mice). **l**, Novel object recognition ($n = 6$ mice). Data are expressed as mean ± s.e.m. $^{*}P < 0.05$, $^{**}P < 0.01$, $^{***}P < 0.001$ and $^{\#}P < 0.0001$, as determined by one-way ANOVA followed by Tukey's multiple comparison test. I.V., intravenous; mo, months; Rel. fold, relative fold; T.Ar, total area.

https://doi.org/10.1038/s43587-024-00694-0

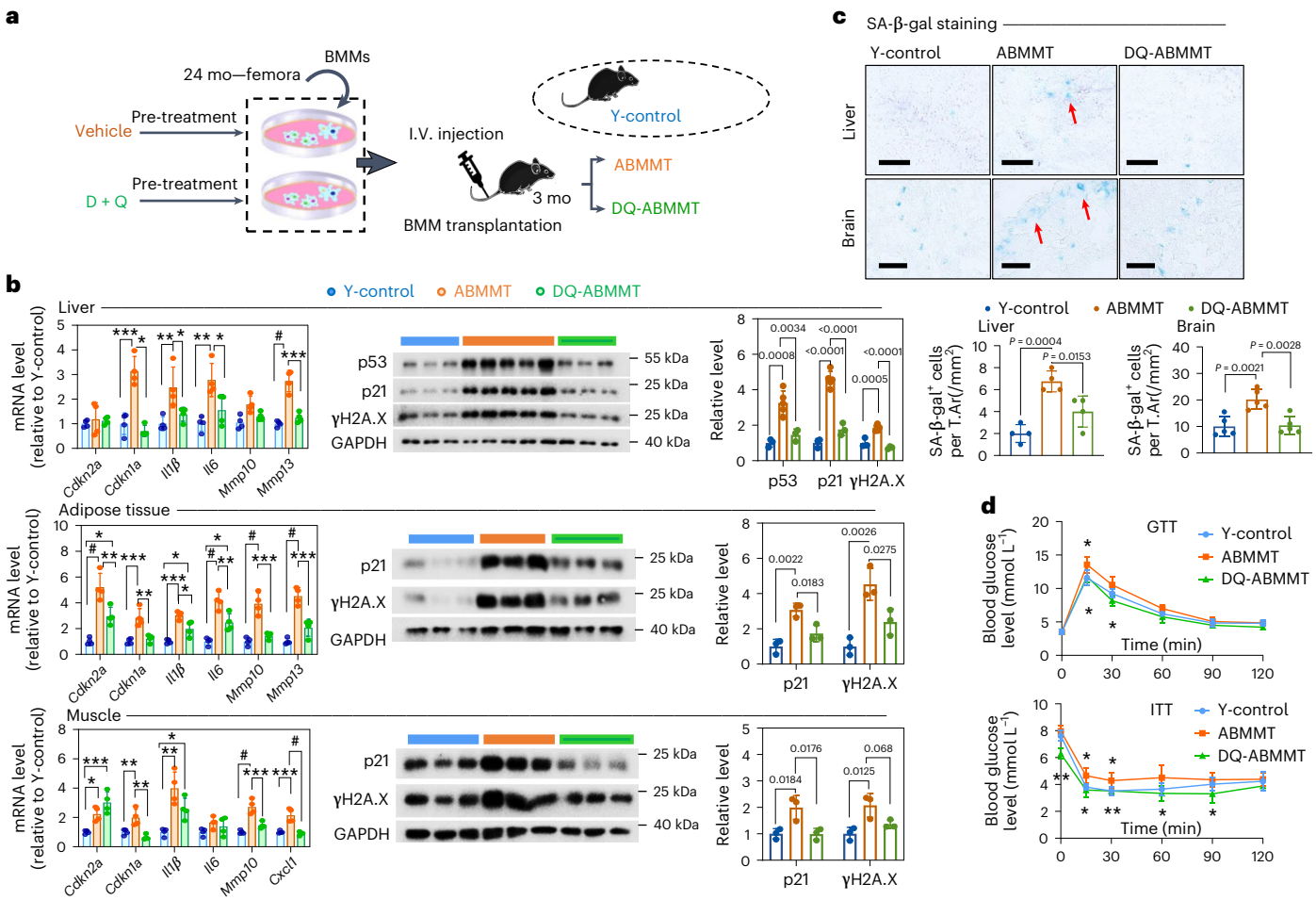

https://doi.org/10.1038/s43587-024-00694-0

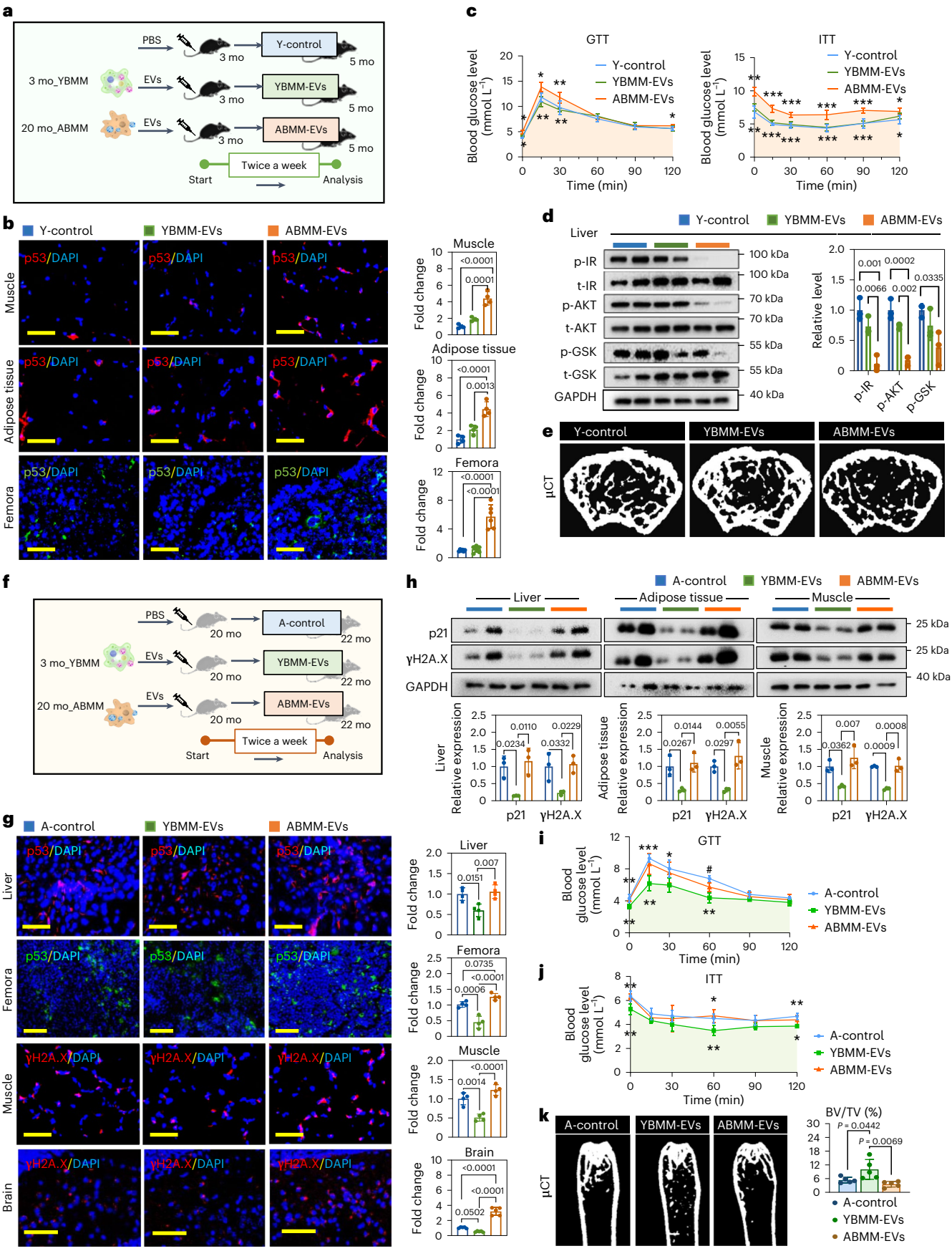

Fig. 4 | EVs secreted by senescent BMMs propagate senescence and aging, whereas YBMM-EVs partially rejuvenate aging. a, Experimental setup for EV transplantation. BMMs were isolated from young mice (3 months old, male) and aged mice (20 months old, male), and EVs secreted by BMMs were collected (YBMM-EVs, ABMM-EVs) and subsequently transplanted into young recipients (3 months old, male mice). **b**, Immunofluorescence staining for p53 in muscle (scale bar, 50 μm; $n = 4$ mice) (upper left), adipose tissue (scale bar, 50 μm; $n = 4$ mice; 5–6 images per mouse) (middle left) and bone sections (scale bar, 50 μm; $n = 6$ mice; 5–6 images per mouse) (bottom left) of young mice treated with YBMM-EVs or ABMM-EVs, and their quantitative analysis (right). **c**, GTT and ITT were performed on young mice receiving adaptive transfer of EVs ($n = 6$ mice). **d**, Phosphorylation level of insulin signaling in liver (left) and quantitative analysis (right) ($n = 3$ mice). **e**, Representative μCT images ($n = 6$ mice). **f**, Outline of the studies. BMMs were isolated from young mice (3 months old, male) and aged mice (20 months old, male), and EVs secreted by BMMs (YBMM-EVs, ABMM-EVs) were collected and subsequently transplanted into aged recipients (20 months old, male mice). **g**, Immunofluorescence detection of p53 in liver (upper left) and femur (middle left) (scale bar, 50 μm; $n = 4$ mice; 5–6 images per mouse) and γH2A.X in muscle (scale bar, 50 μm; $n = 4$ mice; 5–6 images per mouse) (lower left) and brain (scale bar, 50 μm; $n = 5$ mice; 5–6 images per mouse) (bottom left) of aged mice after YBMM-EV or ABMM-EV transplantation, and their quantitative analysis (right). **h**, Protein levels of senescence-related markers in liver (upper left), muscle (middle) and adipose tissue (upper right), and their quantitative analysis (bottom) ($n = 3$ mice). **i**,**j**, GTT (**i**) and ITT (**j**) ($n = 5$ mice). The colored shading in **c**, **i** and **j** represents the area under the curve. **k**, Representative μCT images (left) and quantitative analysis (right) of bone volume/tissue volume (BV/TV) ($n = 5$ mice). Data are presented as mean ± s.e.m. $^{*}P < 0.05$, $^{**}P < 0.01$, $^{***}P < 0.001$ and $^{\#}P < 0.0001$, as determined by one-way ANOVA followed by Tukey's multiple comparison test. mo, months;

transplantation of ABMM-EVs caused young mice to show reduced bone mass, as illustrated by lower trabecular bone volume, compared to the YBMM-EV group (Fig. 4e and Extended Data Fig. 6l,m). These observations support the notion that EVs secreted by senescent BMMs propagate systemic senescence, leading to multi-organ dysfunction.

Young BMM-EVs alleviate aging in multiple tissues

Considering that EVs from senescent BMMs promote systemic senescence and age-related dysfunction, we next explored the possible rejuvenating effects of YBMM-EVs on aged mice. Twenty-month-old mice were treated with YBMM-EVs or ABMM-EVs for 2 months (Fig. 4f). Excitingly, we found that YBMM-EV-treated aged mice showed considerable downregulation or a trend of downregulation of senescence markers in liver, muscle, adipose tissue, bone and brain (Fig. 4g,h and Extended Data Fig. 6n,o). Furthermore, age-related insulin resistance, bone mass loss and decreased Nissl bodies of neurons in aged mice were ameliorated by YBMM-EV treatment (Fig. 4i–k and Extended Data Fig. 6p–r). These data indicate that young BMM-derived EVs partially alleviate aging and aging phenotypes in aged mice.

Altered miRNA levels in BMM-EVs cause age-related disorders

miRNAs are highly enriched in EVs and also in one of the components of SASP[33]. To investigate their possible involvement in the regulation of aging and age-related metabolic disorders, we performed sequencing analysis of miRNAs in YBMM-EVs or ABMM-EVs. Among them, miR-378a-3p (hereafter, miR-378a) and miR-191-5p (hereafter, miR-191) were the most prominently expressed miRNAs in these EVs (Fig. 5a). miR-378a expression was higher in senescent BMMs than young controls (Extended Data Fig. 7a). Moreover, miR-378a expression was elevated in various metabolic tissues of young mice after treatment of ABMM-EVs (Extended Data Fig. 7b). In contrast, miR-191 is more enriched in young BMMs and their derived EVs (Extended Data Fig. 7c). Notably, through miRNA enrichment analysis, we observed that miR-378a and miR-191 were associated with pathways including cellular senescence, insulin signaling pathway and skeletal system development (Extended Data Fig. 7d).

To explore the role of miR-378a-enriched EVs in vivo, we overexpressed miR-378a in macrophage cells and collected the miR-378a-enriched EVs (macrophage-miR378a-EVs) and then transplanted the EVs into young mice (2 months old, male) (Fig. 5b). Excitingly, we found that macrophage-miR378a-EV treatment resulted in higher fasting blood glucose and fasting serum insulin levels (Fig. 5c), increased liver weight to body weight (LW/BW) and serum triglyceride levels (Fig. 5d,e), impaired insulin sensitivity (Fig. 5f,g) and upregulated expression of hepatic lipogenic genes *Fasn* and *Acc1* (Extended Data Fig. 8a) in young recipient mice.

We next tested whether knockout of miR-378a in BMMs could mitigate age-related phenotypes. We constructed miR-378a floxed mice and generated specific knockout of miR-378a in BMMs by intramedullary injection of adeno-associated virus with F4/80 promoter-driven Cre gene (AAV-F4/80-Cre-ZsGreen) (miR-378a-BMM-CKO) (Fig. 5h). Of note, knockout of miR-378a in BMMs downregulated the expression levels of senescence-associated markers and SASP factors in liver, muscle and adipose tissue (Fig. 5i,j and Extended Data Fig. 8b,c). In addition, miR-378a-BMM-CKO mice showed improved blood glucose (Fig. 5k and Extended Data Fig. 8d) and active insulin signaling pathway (Fig. 5l and Extended Data Fig. 8e) and reduced the expression of hepatic gluconeogenic genes (*G6Pase* and *Pepck*) and lipogenic genes (*Fasn* and *Acc1*) (Extended Data Fig. 8f).

Fig. 5 | Role of EV-loaded miRNAs in age-related dysfunction. a, Bar plots show the different miRNA expression in YBMM-EVs and ABMM-EVs. The yellow and green shading represents the candidate miRNAs, namely miRNA-378a-3p (yellow shading) and miRNA-191 (green shading); the green and red horizontal dashed lines represent the expression levels of miRNA-378a-3p in ABMM-EVs (red dashed line) and miRNA-191 in YBMM-EVs (green dashed line). **b**, Outline of the studies (2 months old, male mice). **c**–**e**, Fasting blood glucose ($n = 6$ mice) and fasting serum insulin level (**c**, $n = 5$ mice for control; $n = 4$ mice for other groups), LW/BW (**d**, $n = 5$ mice for 378a-EVs; $n = 4$ mice for other groups) and serum triglyceride levels (**e**, $n = 4$ mice) were measured in young mice transplanted with macropahge-miR378a-EVs. **f**,**g**, GTT (**f**) and ITT (**g**) were performed on young mice treated with macropahge-miR378a-EVs ($n = 9$ mice). **h**, Outline of generating specific knockout of miR-378a in BMMs of miR-378a$^{flox/flox}$ mice (18 months old, male mice). **i**, The mRNA level of senescence-associated markers in muscle ($n = 6$ mice for AAV-Control; $n = 5$ mice for other groups) and adipose tissue ($n = 5$ mice). **j**, Protein levels of senescence markers in liver of miR-378a-BMM-CKO mice (left) and quantitative analysis (right) ($n = 3$ mice). **k**, GTT and ITT were performed on miR-378a-BMM-CKO mice ($n = 6$ mice for AAV-Control; $n = 5$ mice for other groups). The colored shading in **f**, **g** and **k** represents the area under the curve. **l**, Phosphorylation levels of insulin signaling in liver (left) and quantitative analysis (right) ($n = 3$ mice). **m**, Outline of the studies (22 months old, male mice). **n**, Representative SA-β-gal staining of femur from aged mice after infection with AAV-miRNA-191 (scale bar, 50 μm; $n = 5$ mice). The red arrows represent the SA-β-gal-positive cells. **o**,**p**, Representative μCT images (**o**) and quantitative analysis of bone volume/tissue volume (BV/TV) and cortical bone thickness (CT. Th) (**p**) ($n = 12$ mice). **q**, Outline of the studies (2 months old, male mice). **r**, Representative p53 fluorescence staining of femurs after infection with AAV-F4/80-miR-191-sponge (scale bar, 50 μm; $n = 6$ mice) (top) and quantitative analysis (right). **s**, Representative μCT images (left) and quantitative analysis (right) ($n = 6$ mice). Data are expressed as mean ± s.e.m. $^{*}P < 0.05$, $^{**}P < 0.01$, $^{***}P < 0.001$ and $^{\#}P < 0.0001$, as determined by one-way ANOVA followed by Tukey's multiple comparison test in **c**–**g**; two-tailed *t*-test in **i** (muscle and Cdkn1a, Il-6 and Cxcl1 in adipose), **j**–**n**, **p** (CT. Th) and **s**; and two-tailed *t*-test with Welch's correction in **i** (Il-1β in adipose), **p** (BV/TV) and **r**. mo, months; TG, triglyceride; Rel. fold, relative fold; T.Ar, total area.

https://doi.org/10.1038/s43587-024-00694-0

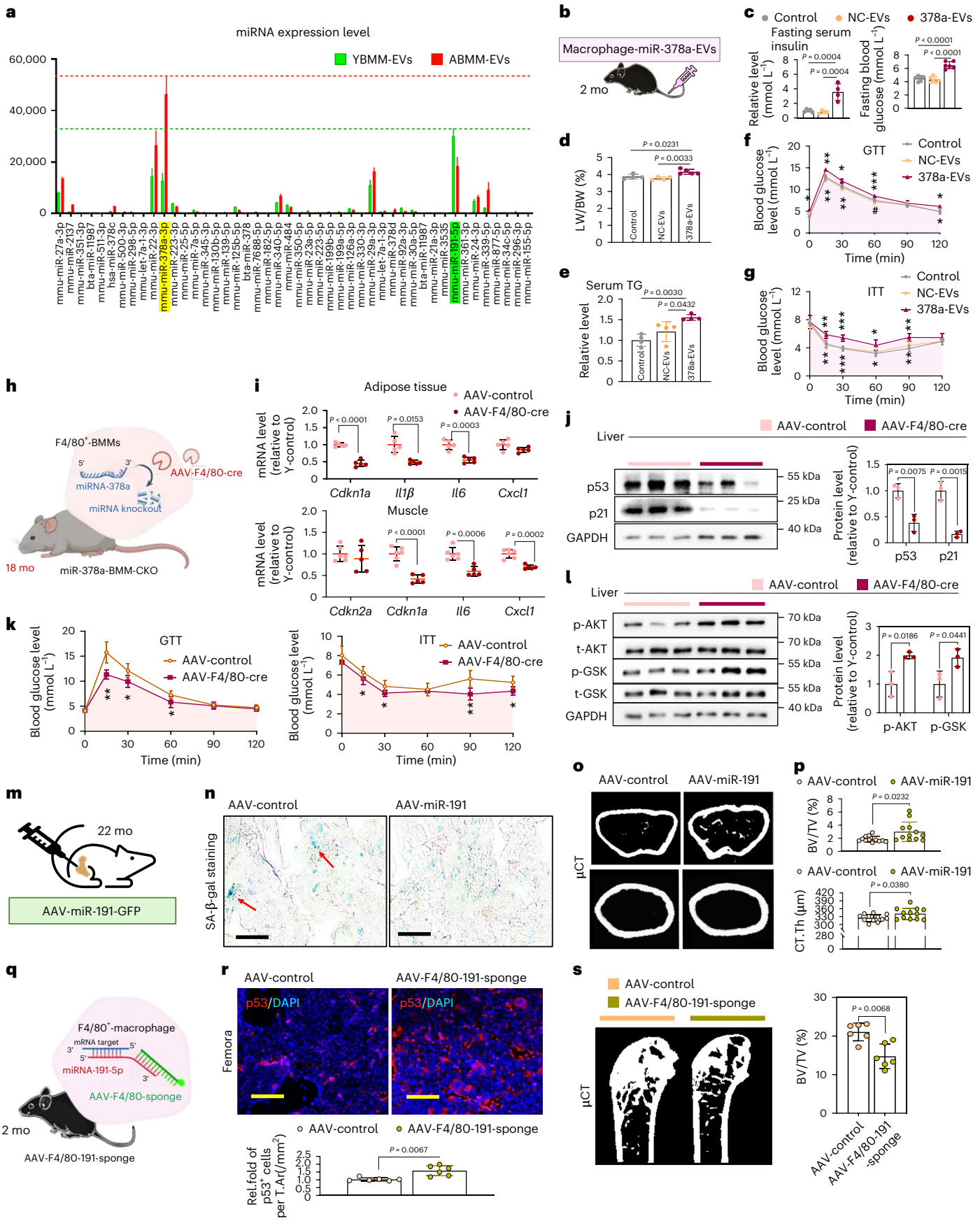

To explore the role of miR-191 in vivo, we overexpressed miR-191 in bone marrow of aged mice (22 months old, male) by intramedullary injection of AAV-miR-191 (Fig. 5m). We observed downregulated SA-β-gal activity, increased trabecular bone mass and elevated cortical bone thickness in aged mice receiving AAV-miR-191 compared to controls (Fig. 5n–p and Extended Data Fig. 8g). We then further investigated whether inhibition of miR-191 expression showed a senescence propagation effect. We used AAV-F4/80-miR-191-sponge to specifically adsorb miR-191 in BMMs of young mice (2 months old, male), thereby achieving a similar effect as knocking out miR-191 (Fig. 5q). Depletion of miR-191 resulted in lower bone mass and more p21 and p53 foci in the bone of young mice (Fig. 5r,s and Extended Data Fig. 8h). In addition, AAV-F4/80-miR-191-sponge-treated mice showed poor performances in muscular strength (grip strength) and physical endurance (hanging test) (Extended Data Fig. 8i).

In addition, we also verified the direct effects of miR-378a and miR-191 on cellular senescence in vitro. We found that overexpression of miR-378a substantially induced the expression of multiple senescence markers (Extended Data Fig. 8j), whereas inhibition of miR-378a expression decreased senescence-associated markers, including SA-β-gal activity in primary hepatocytes (Extended Data Fig. 8k–m). Moreover, we also observed that overexpression of miR-191 reduced SA-β-gal staining and the expression of senescence markers in bone marrow mesenchymal stem cells (BMSCs) (Extended Data Fig. 8n,o).

Together, these observations illustrate that miR-378a and miR-191 could mediate the effects of BMM-EVs in systemic senescence and age-related dysfunction.

Activating peroxisome proliferator-activated receptor α may attenuate age-related disorders in humans

Next, we defined the downstream targets of miR-378a and miR-191. By bioinformatics analysis, among the predicted target genes, we observed peroxisome proliferator-activated receptor α (PPARα), which is known to be involved in lipid metabolism[57], inflammation[58], insulin resistance[59,60], cardiac aging[61] and renal age-associated fibrosis[62]. Through metabolomic analysis of serum from young mice (3 months old) and aged mice (21 months old), we found that the PPAR signaling pathway is substantially inhibited during aging (Fig. 6a,b). Therefore, we further tested the effects of miR-378a and miR-191 on PPARα expression. We found that PPARα abundance in primary hepatocytes, C2C12 cells and 3T3-L1 cells is markedly suppressed with miR-378a overexpression (Fig. 6c and Extended Data Fig. 9a–c). Conversely, inhibition of miR-378a led to a recovery of PPARα protein levels (Extended Data Fig. 9a–c). Interestingly, we found that, upon overexpression of miR-191, PPARα protein level is upregulated (Fig. 6c). Together, these findings demonstrate that both miR-378a and miR-191 may target PPARα to regulate multi-tissue aging.

To test the potential role of PPARα in age-related human disorders, we performed population-based cohort studies using data from the IQVIA Medical Research Database (IMRD), incorporating data from The Health Improvement Network (THIN), a Cegedim database from general practitioners (GPs) in the United Kingdom (UK). We evaluated the risk of type 2 diabetes, major osteoporotic fracture, dementia and all-cause mortality between fenofibrate (a PPARα agonist and a classic clinical lipid-lowering drug) initiators and active comparators (that is, simvastatin users) (Fig. 6d). In total, we identified 1,602 initiators of fenofibrate and 6,384 initiators of simvastatin among participants with pre-diabetes. As shown in Supplementary Table 1, the baseline characteristics, including serum cholesterol and triglyceride levels, of the two matched groups were similar. The risk of type 2 diabetes was lower in the fenofibrate group than in the simvastatin group (Fig. 6e and Table 1). We then compared the risk of secondary outcomes between the two comparison groups. The baseline characteristics for each secondary outcome are shown in Supplementary Tables 2–4, respectively. The risk of major osteoporotic fracture, dementia and all-cause mortality are all lower in the fenofibrate group than in the simvastatin group among participants who were diagnosed with either pre-diabetes or type 2 diabetes (Fig. 6e and Table 1).

Additionally, we estimated life expectancy for patients diagnosed with either pre-diabetes or type 2 diabetes who initiated therapy with fenofibrate or received simvastatin using abridged period life tables based on the Chiang II method[63]. Life tables were constructed from 2000 to 2022, aggregating death and population data into 5-year age intervals up to 90 years. The difference in life expectancy was calculated as the estimated life expectancy in patients treated with simvastatin minus that in patients treated with fenofibrate. Notably, the difference in life expectancy between patients treated with fenofibrate and patients treated with simvastatin increased with age, and fenofibrate consistently exhibited a life expectancy extension across all age groups compared to simvastatin (Fig. 6f and Supplementary Table 5).

Fenofibrate restores tissue homeostasis in aged mice

The results of the above population-based cohort study prompted us to validate the effect of fenofibrate on senescence in vivo (Fig. 7a). Aged mice (23 months old) treated with fenofibrate showed an apparent reduction in senescence-associated markers and SASP factors in liver, muscle, bone and brain compared to controls (Fig. 7b–g). Furthermore, the senescent phenotypes, such as insulin resistance, bone mass loss, decreased physical endurance and poor cognitive function, in aged mice were also partially alleviated by fenofibrate, as reflected by activated insulin pathways (Fig. 7h), better trabecular bone volume (Fig. 7i,j), elevated hanging endurance (Fig. 7k), increased GluR-1 expression (Fig. 7l,m) and improved ability to recognize novel object (Fig. 7n).

In addition, to evaluate whether fenofibrate attenuated age-associated dysfunction and senescence by targeting PPARα, we inhibited PPARα expression in vitro, using primary hepatocytes derived from aged mice (24 months old) and then treated with fenofibrate. We found that fenofibrate decreased SA-β-gal activity alongside multiple other markers of senescence but that these effects were blocked by knocking down PPARα (Extended Data Fig. 9d,e).

These population cohort results, and in vitro and in vivo data, suggest that fenofibrate, in addition to its clinical lipid-lowering effects, may also possess rejuvenative functions, thus delaying aging and age-related diseases.

Discussion

In senescence and aging research, it has remained unclear which cells propagate senescence, driving systemic aging and age-related dysfunction, and whether the propagation of senescence could be prevented. Here we demonstrate that aged BMMs exhibiting phenotypes of senescence themselves drive the propagation of senescence and systemic

Fig. 6 | Fenofibrate delays the onset of age-related disorders in humans. **a**, Outline of the studies. Serum was collected from young mice (3 months old, male) and aged mice (21 months old, male) and subjected to metabolomics analysis. **b**, Differential abundance score shows the changes of metabolites in serum from young and aged mice. The red horizontal line represents the differential enrichment of PPAR signaling pathway in serum from young and aged mice; the red asterisks represent the statistical difference ($P < 0.001$). **c**, Protein levels of PPARα after overexpression of miRNA-378a in primary hepatocytes ($n = 3$ biological replicates) (upper left) or miRNA-191 in BMSCs ($n = 6$ biological replicates) (bottom left), and their quantitative analysis (right). **d**, Outline of the studies. **e**, Cumulative incidence of type 2 diabetes, major osteoporotic fracture, dementia and all-cause mortality in participants initiating fenofibrate and those using simvastatin. **f**, Life expectancy. Data are expressed as mean ± s.e.m. $^{*}P < 0.05$, $^{**}P < 0.01$ and $^{***}P < 0.001$, as determined by two-tailed *t*-test. mo, months.

https://doi.org/10.1038/s43587-024-00694-0

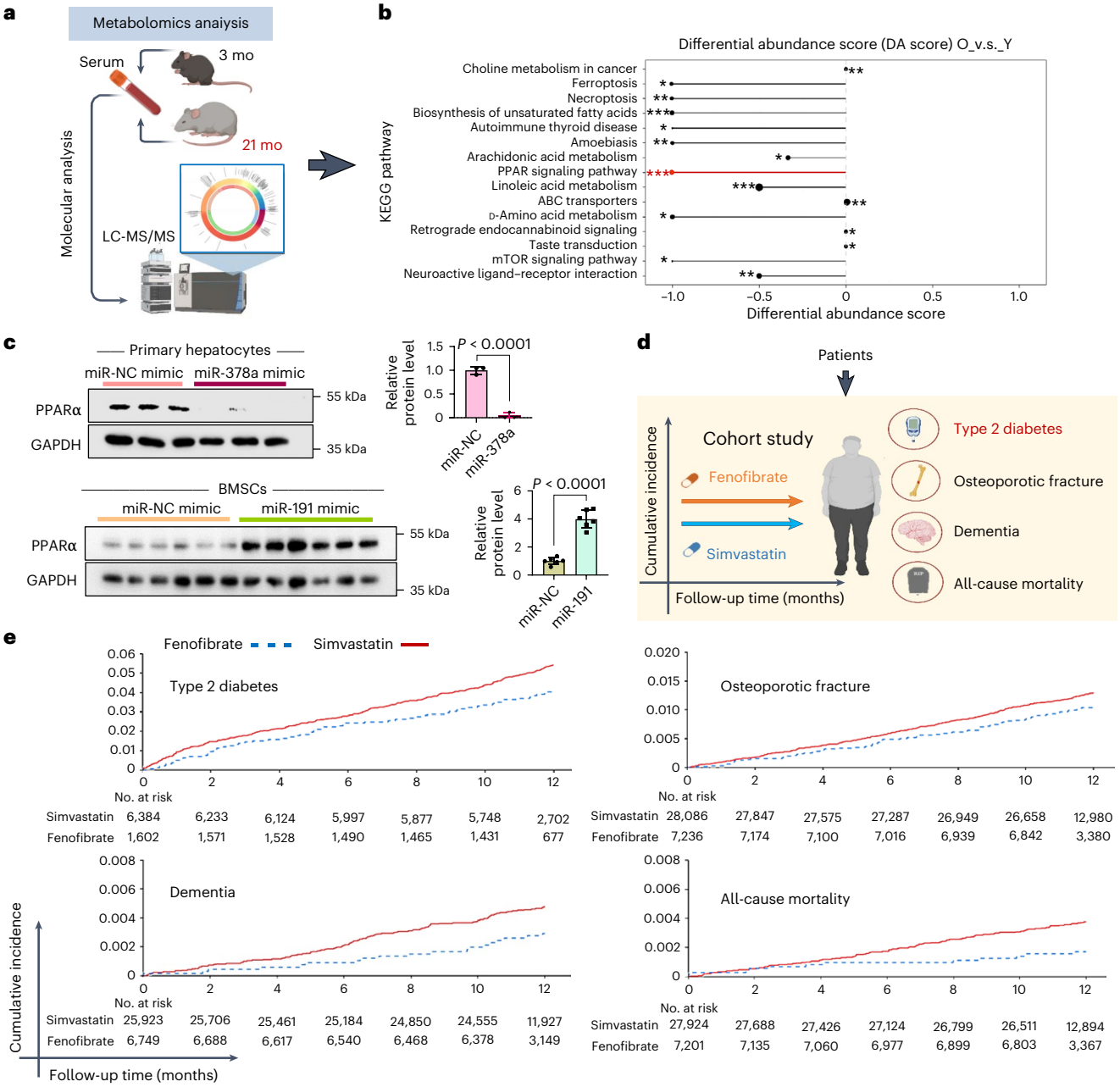

https://doi.org/10.1038/s43587-024-00694-0

Table 1 | Risk of type 2 diabetes, all-cause mortality, major osteoporotic fracture and dementia in participants initiating fenofibrate compared to those using simvastatin

	Fenofibrate	Simvastatin
Incident type 2 diabetes		
Participants[a], *n*	1,602	6,384
Events, *n*	62	335
Mean follow-up (years)	0.93	0.94
Rate of event, per 1,000 person-years	41.4	55.9
RD (95% CI), per 1,000 person-years	−14.5 (−26.4 to −2.6)	0.0 (reference)
HR (95% CI)	0.59 (0.46–0.76)	1.00 (reference)
All-cause mortality		
Participants[b], *n*	7,236	28,086
Events, *n*	73	354
Mean follow-up (years)	0.97	0.97
Rate of event, per 1,000 person-years	10.4	13.0
RD (95% CI), per 1,000 person-years	−2.6 (−5.2 to 0.0)	0.0 (reference)
HR (95% CI)	0.78 (0.60–1.00)	1.00 (reference)
Incident major osteoporotic fracture		
Participants[c], *n*	6,749	25,923
Events, *n*	19	120
Mean follow-up (years)	0.97	0.97
Rate of event, per 1,000 person-years	2.9	4.8
RD (95% CI), per 1,000 person-years	−1.9 (−3.4 to −0.3)	0.0 (reference)
HR (95% CI)	0.51 (0.33–0.81)	1.00 (reference)
Incident dementia		
Participants[d], *n*	7,201	27,924
Events, *n*	12	102
Mean follow-up (years)	0.97	0.97
Rate of event, per 1,000 person-years	1.7	3.7
RD (95% CI), per 1,000 person-years	−2.0 (−3.3 to −0.8)	0.0 (reference)
HR (95% CI)	0.51 (0.29–0.89)	1.00 (reference)

RD, rate difference; HR, hazard ratio; 95% CI, 95% confidence interval. [a]Including participants with pre-diabetes. [b]Including participants with pre-diabetes and type 2 diabetes. [c]Including participants with pre-diabetes and type 2 diabetes and excluding those with a history of major osteoporotic fracture. [d]Including participants with pre-diabetes and type 2 diabetes and excluding those with a history of dementia.

aging, via EVs. Our population cohort data and in vivo studies in mice suggest that fenofibrate may delay age-related disease by antagonizing pro-aging effects of senescent BMMs, and we propose fenofibrate as a candidate therapy to alleviate age-associated diseases and extend healthy lifespan (Extended Data Fig. 10).

Studies have shown that senescence and aging are systematically propagated[64,65]. Intraperitoneal transplantation of small numbers (0.5×10^6–1×10^6) of senescent pre-adipocytes was found to be sufficient to induce physical dysfunction in young mice[66]. In our study, the transplantation of aged bone marrow cells (2×10^6) and senescent BMMs (2×10^6) could drive the propagation of senescence from old to young mice. One reason why such a small number of transplanted senescent cells may lead to systemic dysfunction is the spread of senescence in local and distant tissues. Moreover, healthy hypothalamic stem/progenitor cells[42] and young fibroblasts[39] have been reported to ameliorate senescence in a variety of tissues in aged mice by releasing EVs. Thus, we reasoned that these senescent cells may affect non-senescent cells in local and distant tissues through the simultaneous contribution of multiple mechanisms, including EVs, soluble molecules and SASP. In addition, although these senescent cells are shown to contribute to paracrine senescence, which cell type primarily drives systemic aging, whether crosstalk exists between these senescent cells and how they interact with each other require further exploration and research.

As exemplified by blood exchange or old plasma dilution[18,67–70], blood-borne factors are thought to be pro-rejuvenative[71] or pro-aging. Old mice exposed to young circulatory milieu experience systemic rejuvenation, whereas young recipient mice exhibit an increased senescence burden after receiving old blood exchange[55,72]. However, the molecular identities and origins of these functional blood-borne factors remain elusive. EVs appear in various body fluids and function in both physiological and pathological conditions[32,73]. Injection of serum EVs from young animals improves the outcome of ischemic stroke and downregulates age-associated molecule expression[74–76]. Conversely, aged serum EVs aggravate sensorimotor deficits[77]. Despite these findings, the origin of these serum EVs, which may be candidate blood-borne factors, remains unknown. In this study, we establish that EVs released by senescent BMMs possess pro-aging properties, whereas young BMM-derived EVs exhibit certain rejuvenating effects on multiple distant tissues, indicating that BMM-derived EVs are, at least partially, responsible for the modulatory effects of serum EVs on aging.

Currently, there exist some interventions[78–80] or drugs that can partially alleviate aging and age-related metabolic disorders[81–84]. Among these, rapamycin and D+Q have shown promising results in animal models through targeting the mTOR signaling pathway and cellular senescence, respectively[85,86]. However, because the mTOR pathway is extensively involved in numerous essential physiological processes, many reported adverse reactions are caused by using rapamycin, including hyperglycemia, dyslipidemia, acute nephrotoxicity and delayed wound healing[87]. Clinical trials have demonstrated that short-term D+Q treatment reduces senescent cells and enhances physical function in patients with conditions such as diabetic kidney disease or idiopathic pulmonary fibrosis[51,88]. However, the long-term safety and efficacy of D+Q treatment have yet to be clinically proven. Here, our study unveils another innovative therapeutic strategy for reducing

Fig. 7 | Fenofibrate effectively restores tissue homeostasis in aged mice. **a**, Experimental setup for fenofibrate treatment. Aged mice (23 months old) were treated with vehicle or fenofibrate (A-vehicle, A-fenofibrate), and then the senescent phenotypes were assessed. **b**,**c**, Gene expression of senescence and SASP markers in liver ($n = 4$ mice) (**b**) and brain ($n = 4$ mice for Y-vehicle; $n = 3$ mice for other groups) (**c**) of aged mice treated with fenofibrate. Color bars are the heatmap of relative mRNA expression. **d**,**e**, Protein expression of p21 and γH2A.X in liver and muscle (**d**) and their quantitative data (**e**) ($n = 3$ mice). **f**,**g**, Immunofluorescence detection of γH2A.X in liver and brain (**f**) and their quantitative data (**g**) (scale bar, 50 μm; $n = 4$ mice; 5–6 images per mouse). **h**, Phosphorylation levels of insulin signaling in liver (upper left) and muscle (upper right), and their quantitative analysis (bottom) ($n = 3$ mice). **i**,**j**, Representative μCT images (**i**) and quantitative analysis of bone volume/tissue volume (BV/TV) (**j**) ($n = 4$ mice). **k**, Hanging endurance ($n = 4$ mice). **l**,**m**, Immunofluorescence detection of GluR-1 in brain (**l**) and quantification of GluR-1 foci (**m**) (scale bar, 50 μm; $n = 4$ mice; 5–6 images per mouse). **n**, Novel object recognition ($n = 4$ mice). Statistical differences were determined by one-way ANOVA followed by Tukey's multiple comparison test. mo, months; Rel. fold, relative fold; T.Ar, total area.

https://doi.org/10.1038/s43587-024-00694-0

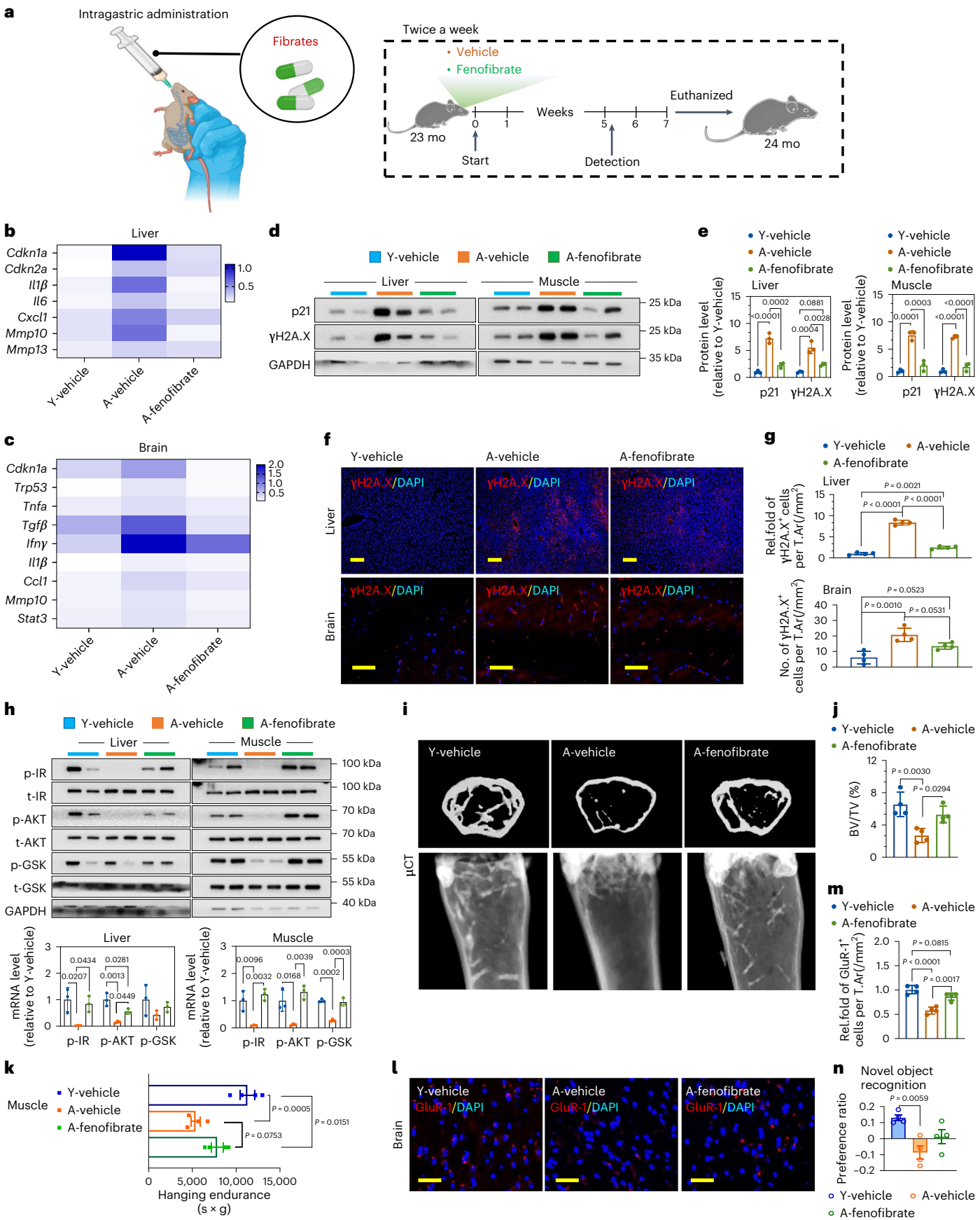

senescent cells and mitigating age-related diseases through targeting PPARα by an FDA-approved and clinically available lipid-lowering drug, fenofibrate. In humans, fenofibrate has been studied extensively and has been in clinical use for nearly 50 years with a high safety profile[89,90]. Further research and clinical studies will be needed to demonstrate the safety and effectiveness of fenofibrate in targeting aging and several age-related human morbidities.

One limitation of this study is the use of male mice. To avoid the potential confounding bias of estrogen deficiency on systemic aging and osteoporosis, we used male mice in this study. Although our cohort study of 7,986 participants included an approximately 40% female population, showing that fenofibrate mitigates age-related diseases, whether aged BMMs also induce paracrine senescence and age-related dysfunction in female mice was not tested in this study. Future study is needed to investigate the role of aged BMMs in systemic aging using a female animal model.

Methods

Mouse models and ethics

Wild-type (WT) male C57BL/6 mice were purchased from the SLAC Laboratory Animal Company of Hunan Province and maintained in a specific pathogen-free (SPF) environment until the age of 16–24 months. For D+Q treatment, 16-month-old WT mice were randomly divided into two groups and were given vehicle (PEG 400) or Dasatinib (5 mg kg^{-1}, LC Labs, D-3307) plus Quercetin (50 mg kg^{-1}, Sigma-Aldrich, Q4951) by gavage twice a week for 5 months[48,86]. For fenofibrate treatment, aged WT mice (23 months old) were given vehicle or fenofibrate (100 mg kg^{-1} d^{-1}, Sigma-Aldrich, F6020) by gavage daily for 5 weeks. miR-378a floxed heterozygous mice were generated by Nanjing GemPharmatech Co., Ltd., and homozygous mice were obtained by crossing. The genotypes of the mice were determined by polymerase chain reaction (PCR) analysis of DNA extracted from mouse tail using the following primers: 5′ arm forward, CAC TTG CTG CCG TAC TTT CAC G, and reverse, CCA ACT GAC CTT GGG CAA GAA CAT; 3′ arm forward, TAC TCT TGC CGT TCA TGT GCG, and reverse, AAG ATG GCT CCT ACC AAA GGT AGC.

All animal care protocols and experiments were reviewed and approved by the Animal Care and Use Committee of the Laboratory Animals Research Center, Xiangya Medical School, Central South University, under active protocol 2019030214. Mice were kept at 20–24 °C with a 12-h light/dark cycle, and all mice were provided with food and water ad libitum. Room temperature was 20–26 °C; daily temperature difference was ≤4 °C; and relative humidity was 40–70%.

Scientific and ethical approval of human data and the statement are described below. The scientific review committee for the IMRD and the institutional review board at Xiangya Hospital approved this study, with a waiver of informed consent (23SRC020, 2018091077). THIN is a registered trademark of Cegedim SA in the UK and other countries. Reference made to the THIN database is intended to be descriptive of the data asset licensed by IQVIA. This work uses de-identified data provided by patients as a part of their routine primary care.

Cell isolation and culture

BMM isolation. Mouse BMMs were isolated as described previously[23]. In brief, WT male mice were euthanized, and femurs and tibias were removed and flushed with α-MEM essential medium (Gibco). Bone marrow cells were cultured overnight in α-MEM medium containing 10% FBS. Then, we discarded the adherent cells and cultured the floating cells with 30 ng ml^{-1} M-CSF (Proteintech, HZ-1192) to obtain monocytes/macrophages.

Primary hepatocyte isolation. Primary mouse hepatocytes were harvested as previously described[91]. In brief, male mice were anesthetized with pentobarbital, and the digestive solution was perfused into the inferior vena cava to obtain primary hepatocytes. Primary hepatocytes were cultured in DMEM medium containing 10% FBS (Gibco)[91].

Mouse myoblast cell line C2C12 and mouse pre-adipocyte cell line 3T3-L1 were purchased from Procell Life Science & Technology Co., Ltd. (CL-0006 and CL-0044). All cells were grown in a cell incubator at 37 °C and 5% CO_2.

Bone marrow transplantation

Bone marrow transplantation was performed as described previously[92,93]. In brief, recipient mice were irradiated with lethal dose (PXI, X-RAD 225 OptiMAX, 9.5 Gy, in two split doses) and then subcutaneously injected with 1 ml of normal saline. The donor mice were euthanized, and femurs and tibias were dissected and flushed with cold PBS. The obtained cell suspension was filtered through a 100-μm cell filter and counted using a cell counter. Three hours after irradiation, bone marrow cells (2×10^6 per mouse) were transplanted into recipient mice via tail vein. Irradiated recipient mice required a recovery period of approximately 45 d.

For transplantation efficiency assay, mouse blood was taken from the tail vein, and approximately 100 μl of peripheral blood was collected in EDTA tubes. The collected blood was resuspended in 10 times the volume of red blood cell lysis buffer and lysed for 10 min. Cells were incubated with APC-anti-mouse-CD45.2 (Invitrogen, 17-0454-82, 1:20) and FITC-anti-mouse-CD45.1 (Invitrogen, 11-0453-82, 1:50). Stained cells were collected by BD FACSDiva software version 9.0 and a BD flow cytometry FACSCanto II system. Data were analyzed by FlowJo version 10 (BD Biosciences). Dead cells were removed by dead cell dye staining and FSC-A/FSC-H gating, and then the gate (CD45.1: FITC; CD45.2: APC) was set to further analyze the stained cells.

Bioinformatics analysis of scRNA-seq data

(1) Primary analysis of raw read data. Raw reads (Gene Sequence Archive (GSA): CRA004660) were processed with FastQC and fastp to remove low-quality reads[55]. (2) Cells were separated into clusters by the normalized expressions of the following canonical markers[94,95]: granulocyte–macrophage progenitor (GMP) cells (MS4A3, Elane, Mpo and Prtn3); monocyte–macrophages (Fos, Csf1r, Csf3r, Cebpb, Lyz2, Cd68, Cd163 and Adgre1); dendritic cells (Cd74 and Irf8); plasma cells (Cd79b, Jchain and Mzb1); B cells (Cd79b, Cd19Dntt, Rag1 and Ezh2); T cells (Cd3d, Cd8a and Nkg7); T cell_Bcl2_hi (Cd3, Cd4, Cd8 and Bcl2); basophils (Ms4a2 and Cd63); common myeloid progenitors (c-Kit, Cd34, Lin and Sca1); stage1_neutrophils (Camp, Ngp, Ltf, Fcnb, Tuba1B, Chil3, Mpo, Prtn3, Elane, Rpl12, Sox4 and Cd34); stage2_neutrophils (Srgn, Ccl6, Csf3r, Clec7a, Clec4d, Ifit3, Pla2g7, Dusp1, Qasl2, H2Q10, Rsad2, Gm11428, Cd300ld, Sirpb1a and 2010005H15Rik); erythroid cells (Rhd, Gypa, Rhag, Car2 and Hba-a1); hematopoietic stem and progenitor cells (HSPCs) (Vcp, Pdap1, Mrpl34 and Eif3c); mesenchymal stem cells (Cd74, Cd81, Tbxas1 and Rtp4); and natural killer (NK) cells (NKG7, GZMA, GZMB and IL2RB). (3) Differentially expressed gene (DEG) analysis. Genes expressed in more than 10% of the cells in a cluster and with average log (fold change) of greater than 0.25 were selected as DEGs by Seurat FindMarkers (version 3.1.2) based on Wilcoxon likelihood-ratio test with default parameters. (4) Pathway enrichment analysis. KEGG analysis was used with the 'clusterProfiler' R package version 3.5.1. Pathways with adjusted *P* value less than 0.05 were considered significantly enriched.

BMM transplantation

Donor mice were euthanized, and the femurs and tibias were removed and flushed with α-MEM essential medium (Gibco). The obtained cell suspension was filtered, centrifuged and transferred to Petri dishes for overnight culture. The adherent cells were then discarded, and floating cells were cultured with 30 ng ml^{-1} M-CSF. Mature macrophages were harvested and transplanted into recipient mice via tail vein (2×10^6 per mouse)[92,96,97].

After 3 d of culture, macrophages isolated from aged mice (24 months old) were treated with DMSO or D+Q (D: 0.2 μmol L^{-1}, Q: 20 μmol L^{-1}) for 24 h, and then the medium was changed for recovery

for 1 d. Macrophages were harvested and subsequently transplanted into recipient mice[66,84,98].

EV purification and characterization

EV purification, identification and treatment were performed according to previously described protocols[29,30]. In brief, after 72-h BMM culture, debris and dead cells in the medium were removed by centrifugation at 1,000*g* for 10 min and then filtrated through a 0.22-μm filter. The harvested supernatant was centrifuged with filters (100 kDa), and the EV-containing pellet was resuspended in PBS. The characterization of EVs was confirmed by the expression of EV-associated protein markers TSG101 and CD9 (by western blot), EV morphology (by electron microscopy) and EV particle size (by nanoparticle tracking analysis (NTA)). The collected EVs were transplanted into recipient mice through tail vein twice a week for 2 months.

miRNA microarray assay

To identify the differently expressed miRNAs in the EVs released by macrophages from aged mice (18 months old) and young mice (3 months old), miRNA microarray assays were performed with the help of Obio Technology. The accession numbers for the sequencing data reported in this paper are Sequence Read Archive (SRA): SRR28495907–SRR28495911.

Metabolomic analysis

To identify the differently expressed metabolites in the serum from aged mice (22 months old) and young mice (3 months old), metabolomic analysis was performed with the help of Biotree Biomedical Technology Co., Ltd. Metabolic pathway enrichment analysis of differential metabolites was performed based on the KEGG database. Metabolic pathways with $P < 0.05$ were significantly enriched by differential metabolites. The accession number for the sequencing data reported in this paper is Open Archive for Miscellaneous Data (OMIX): OMIX006114.

AAV recombination

To specifically knock down miR-378a in BMMs, we used the AAV2 viral vector to deliver macrophage-specific AAV2-F4/80-Cre into BMMs of homozygous mice (miR-378a$^{flox/flox}$ mice) by intramedullary injection. AAV2-F4/80-Cre viral titer of 1.3×10^{12} vector genomes per milliliter (vg/ml) and AAV2-F4/80-Cre viral titer of 1.3×10^{12} vg/ml were used in this study. For local delivery, 30 μl of AAV2-F4/80-null or AAV2-F4/80-Cre was intraosseously injected into the bone marrow of miR-378a$^{flox/flox}$ mice[97].

Similarly, overexpression of miR-191-5p was achieved by injecting AAV-miR-191-5p into the bone marrow cavity of 22-month-old C57BL/6 mice.

In addition, AAV-F4/80-miR-191-5p-sponge was constructed to specifically adsorb miR-191-5p from BMMs in 2-month-old C57BL/6 mice. The amount of virus injected was according to the manufacturer's instructions (HANBIO).

qRT–PCR

Total RNA from cells or tissues was extracted using TRIzol reagent (Accurate Biology) according to the manufacturer's protocol. After reverse transcription using Evo M-MLV RT Master Mix (AG11706), cDNA was quantified in an ABI real-time system (Applied Biosystems). For miRNA detection, total RNA was reverse transcribed with an All-in-One miRNA First-Strand cDNA Synthesis Kit (GeneCopoeia, QP113) and subsequently measured by real-time PCR with miR-378a-3p-specific or miR-191-5p-specific primers (GeneCopoeia, QP115). All primer sequences used are presented in Supplementary Table 6.

Western blot

Cells or tissues were lysed in RIPA lysis buffer containing protease inhibitors and phosphatase inhibitors. Samples were loaded into electrophoresis gels, separated by SDS-PAGE and electro-transferred to PVDF membranes. After blocking with 5% skim milk, PVDF membranes were incubated with primary antibodies and incubated overnight on a shaker at 4 °C. Then, secondary antibodies were incubated for an additional hour at room temperature. All antibodies used are shown in Supplementary Table 6. The protein levels were visualized using Image Lab (Bio-Rad, version 6.1) and the ChemiDoc XRS Imaging System (Bio-Rad).

Immunofluorescence and immunohistochemical staining

Liver, muscle, adipose tissue, femur and brain were fixed overnight in 4% paraformaldehyde, and then the liver, muscle, adipose tissue and brain were embedded with cryo-embedding medium (2% polyvinylpyrrolidone, 20% sucrose and 8% gelatin contained in 1× PBS). The femurs were decalcified with 0.5 M EDTA before embedding in cryo-embedding medium. Tissue cryosections were blocked with 3% BSA and stained with primary antibodies overnight: γH2AX (1:100 dilution, Santa Cruz Biotechnology, sc-517348), p21 (1:100 dilution, Santa Cruz Biotechnology, sc-6246), p53 (1:500 dilution, Cell Signaling Technology, 2524s), F4/80 (1:200 dilution, Abcam, ab6640), OCN (1:300 dilution, Takara Bio, M137), PSD-95 (1:100 dilution, Santa Cruz Biotechnology, sc-32290), GluR-1 (1:100 dilution, Santa Cruz Biotechnology, sc-55509) and IBA1 (1:100 dilution, Proteintech, 10904-1-AP). Subsequently, fluorescence-conjugated secondary antibodies Alexa Fluor 488–conjugated anti-rabbit (Invitrogen, A21206, 1:200) or Alexa Fluor 555–conjugated anti-rabbit (Invitrogen, A21428, 1:200) or Alexa Fluor 555–conjugated anti-mouse (Invitrogen, A31570, 1:200) were used.

For immunohistochemical staining, muscle, adipose tissue and bone tissue sections were incubated overnight with primary antibodies: OCN (1:400 dilution, Takara Bio, M137), p21 (1:100 dilution, Santa Cruz Biotechnology, sc-6246) and p53 (1:500 dilution, Cell Signaling Technology, 2524s). Finally, the nuclei were stained with hematoxylin. The images of staining were quantified using ImageJ 1.52 software.

SA-β-gal staining

Senescent cells were detected using a Senescence-Associated β-Galactosidase Staining Kit (Solarbio, G1580) according to the manufacturer's instructions. Tissue cryosections or cells were placed in a 37 °C incubator overnight after adding the staining working solution. The staining was observed under an ordinary light microscope.

Glucose tolerance test and insulin tolerance test

Glucose tolerance test (GTT) was performed on mice fasted for 12 h. After fasting blood glucose was measured, blood glucose levels were detected at 15 min, 30 min, 60 min, 90 min and 120 min after intraperitoneal injection of glucose solution (1 g kg^{-1}). Insulin tolerance test (ITT) was performed after a 4-h fast, with intraperitoneal injection of insulin (0.75 U kg^{-1}) and measurement of glucose levels at designated timepoints[99].

Insulin signaling analysis

Phosphorylation of the insulin pathway stimulated by insulin in vivo was carried out as described previously[91,99]. In brief, after fasting for 8 h, mice were anesthetized, and parts of liver, skeletal muscle and adipose tissue were collected at 3 min, 7 min and 10 min after injection of insulin (1 U kg^{-1} body weight) through portal vein. Western blot analysis was used to detect the phosphorylation of insulin pathway.

Grip strength

Forelimb grip strength was measured by a paw grip strength tester (BIOSEB). After grasping the metal grid, the mice were pulled backward in the horizontal direction. The value displayed on the instrument is the grip strength of the mice. Results were averaged over six trials[16].

Hanging test
Mice were placed on metal web and allowed to grasp the web with both forelimbs and hind limbs. The time for the mice to fall from the web was recorded. Three trials were performed for each mouse, and the results were averaged[18].

Microcomputed tomography analysis
For microcomputed tomography (μCT) analysis of femoral bones, high-resolution μCT was used (SKYSCAN 1172, Bruker MicroCT). NRecon image reconstruction software (version 1.6), CTVol three-dimensional model visualization software (Bruker MicroCT, version 2.0) and data analysis software (CT Analyzer, version 1.9) were used to analyze the trabecular bone parameters (BV/TV, Tb.Th, Tb.N and Tb.Sp)[23,100,101].

Oil Red O staining
Liver 8-μm cryosections were stained with Oil Red O staining reagent (HyCyte) for 30 min, and nuclei were stained with hematoxylin. Sections were washed with deionized water and sealed in glycerin gelatin.

Triglyceride measurement
Serum and hepatic triglyceride levels were determined according to the manufacturer's instructions (Elabscience). In brief, 20 mg of liver tissue was homogenized in isopropanol, and centrifuged supernatants were collected. The obtained liver supernatant and serum were subjected to enzymatic measurement using kits.

Data source of population-based cohort
We used data from IMRD, incorporating data from THIN, a Cegedim database from GPs in the UK. IMRD contains anonymized medical records from 839 general practices with approximately 19 million patients. Healthcare information is recorded at each practice on socio-demographics, anthropometrics, lifestyle factors, visits to GPs, diagnoses from specialists, hospital admissions and laboratory test results. A previous study demonstrated the validity of the IMRD database in clinical and epidemiological research[102]. The scientific review committee for the IMRD and the institutional review board at Xiangya Hospital approved this study, with a waiver of informed consent (23SRC020, 2018091077).

Study design and cohort definition
We included individuals who were aged 40–90 years, were diagnosed with pre-diabetes and had at least 1 year of active enrollment with the general practice from January 2000 to December 2022. Pre-diabetes was defined by baseline impaired fasting blood glucose (5.6–6.9 mmol L^{-1}), impaired glucose tolerance (GTT result, 7.8–11.0 mmol L^{-1}), HbA1c of 5.7–6.4% or a combination of these results[103]. To improve the robustness of observational analysis, we followed the target trial emulation design framework[104,105] and adopted a prevalent new user design[106–108] to compare the risk of incident type 2 diabetes between fenofibrate initiators and active comparators (that is, simvastatin users). We assembled a study cohort including patients initiating therapy with fenofibrate or receiving simvastatin during the study period and then stratified the fenofibrate users into two types: those who switched to fenofibrate (also called prevalent new users) and those who were incident new users. We considered the switching date or date of incident use as the index date. For each prevalent new user, we matched up to five individuals who continued simvastatin and had used the simvastatin for the same duration at the time of the index date. For each incident new user, we matched up to five incident new users of simvastatin. We excluded patients who were diagnosed with diabetes before the index date.

To assess the extra benefits of fenofibrate, we also examined the relation of fenofibrate initiation to the risk of several secondary outcomes, including all-cause mortality, incident major osteoporotic fracture (hip, vertebral, wrist and humerus fracture) and incident dementia among individuals who were diagnosed with either pre-diabetes or type 2 diabetes.

Assessment of outcomes
The primary outcome was incident type 2 diabetes. We defined type 2 diabetes using Read codes. This approach was used in the previous study[109]. The event date was defined by the date of diagnosis. Secondary outcomes included all-cause mortality, incident major osteoporotic fracture (hip, vertebral, wrist and humerus fracture) and incident dementia. The death date recorded in THIN is linked to the National Health Service; thus, a change in vital status to 'dead' is immediately updated in the individual's electronic health record. Major osteoporotic fracture (hip, vertebral, wrist and humerus fracture) and dementia were identified by the Read codes, respectively, which were used in previous studies by using the IMRD database[110,111].

Additionally, we estimated life expectancy for patients diagnosed with either pre-diabetes or type 2 diabetes who initiated therapy with fenofibrate or received simvastatin using abridged period life tables based on the Chiang II method[63]. Life tables were constructed from 2000 to 2022, aggregating death and population data into 5-year age intervals up to 90 years. The difference in life expectancy was calculated as the estimated life expectancy in patients treated with simvastatin minus that in patients treated with fenofibrate.

Assessment of covariates
Covariates included sociodemographic factors (age, sex and socioeconomic deprivation index score), body mass index (BMI), lifestyle factors (alcohol use and smoking status), comorbidities (hypercholesteremia, hypertriglyceridemia, hypertension, transient ischemic attack, ischemic heart disease, myocardial infarction, stroke, osteoarthritis, chronic kidney disease, depression, varicose veins, venous thromboembolism, chronic obstructive pulmonary disease, pneumonia or infection, osteoporosis, fall and cancer) before the index date, medication use (non-steroidal anti-inflammatory drugs (NSAIDs), opioids, other statins, corticosteroids, thiazide diuretics, anti-hypertensives, anti-diabetics, anti-coagulants, aspirin, anti-depressants, proton pump inhibitors, benzodiazepine, warfarin, anti-osteoporosis drugs, nitrates and bisphosphonates) and healthcare use during 1 year before the index date. Missing values were treated as a separate missing category for each variable.

Statistical analysis of population-based cohort
We performed conditional logistic regression separately for the incident new users and prevalent new users and stratified by cluster to calculate conditional propensity scores for the initiation of fenofibrate. The propensity scores predict the probability of treatment with fenofibrate versus simvastatin based on baseline covariates. We matched patients treated with fenofibrate chronologically (starting with the patient with the earliest calendar date) using a variable ratio one to many (1:5) nearest neighbor matching within a caliper of 0.2 standard deviations of the propensity scores to individuals treated with simvastatin in each cluster[112]. Thus, we created two groups of participants with the same distribution of all known baseline characteristics, such as age, sex, treatment history and other potential confounders, emulating the randomization process of a hypothetical trial[105].

In the conditional propensity scores matching cohort, for each patient, we calculated person-years of follow-up as the amount of time from the index date to the first of the following events: incident type 2 diabetes during the 1 year of follow-up, death, 1-year follow-up, transferring out of the GP practice and end of the study (31 December 2022). We plotted the cumulative incidence curve for type 2 diabetes and fitted a Cox proportional hazards model to estimate the hazard ratio, accounting for the competing risk of death and matched study design[113]. We repeated the analyses for the secondary outcomes, respectively. For all

analyses, missing values for covariates (for example, smoking status, alcohol use and BMI) were adopted as a missing indicator approach, whereby missing categories were included in the analysis.

All *P* values were two-sided, and $P < 0.05$ was considered significant for all tests. All statistical analyses were performed with SAS software version 9.4 (SAS Institute).

Statistics and reproducibility

All data were analyzed using Excel (Microsoft) and Prism 8 (GraphPad) software. In bar graphs, data are expressed as mean values ± s.e.m. Statistical significance ($P < 0.05$) was computed using two-tailed Student's *t*-test, Welch's *t*-test or one-way ANOVA followed by Tukey's multiple comparison test, as indicated in the figure legends. *n* represents the number of samples used in the experiments. No statistical method was used to predetermine sample size, but our sample sizes are similar to those reported in previous publications[21,23]. No animals or data were excluded from the analyses. No randomization method was used. The investigators were not blinded to allocation during experiments and outcome assessments, but the experiments were performed in appropriate biological replication by independent personnel to avoid bias. All micrographs and blots were representative of at least three independent experiments. Data distribution was assumed to be normal, but this was not formally tested.

Reporting summary

Further information on research design is available in the Nature Portfolio Reporting Summary linked to this article.

Data availability

Raw data of the metabolomic analysis have been deposited in the Genome Sequence Archive in the National Genomics Data Center, China National Center for Bioinformation, under accession code OMIX006114 (https://ngdc.cncb.ac.cn/omix/releaseList). Raw data of RNA sequencing have been deposited in the Sequence Read Archive (https://www.ncbi.nlm.nih.gov/sra) under accession codes SRR28495907–SRR28495911. Source data are provided with this paper. All other data are available from the corresponding authors upon reasonable request.

References

1. Pan, C. C. et al. Antagonizing the irreversible thrombomodulin-initiated proteolytic signaling alleviates age-related liver fibrosis via senescent cell killing. *Cell Res.* **33**, 516–532 (2023).
2. Grosse, L. et al. Defined $p16^{High}$ senescent cell types are indispensable for mouse healthspan. *Cell Metab.* **32**, 87–99 (2020).
3. Baker, D. J. et al. Clearance of $p16^{Ink4a}$-positive senescent cells delays ageing-associated disorders. *Nature* **479**, 232–236 (2011).
4. Wagner, J. U. G. et al. Aging impairs the neurovascular interface in the heart. *Science* **381**, 897–906 (2023).
5. Khosla, S., Farr, J. N. & Monroe, D. G. Cellular senescence and the skeleton: pathophysiology and therapeutic implications. *J. Clin. Invest.* **132**, e154888 (2022).
6. Farr, J. N. et al. Identification of senescent cells in the bone microenvironment. *J. Bone Miner. Res.* **31**, 1920–1929 (2016).
7. Tuttle, C. S. L. et al. Cellular senescence and chronological age in various human tissues: a systematic review and meta-analysis. *Aging Cell* **19**, e13083 (2020).
8. Zhang, L. et al. Cellular senescence: a key therapeutic target in aging and diseases. *J. Clin. Invest.* **132**, e158450 (2022).
9. Saul, D. & Khosla, S. Fracture healing in the setting of endocrine diseases, aging, and cellular senescence. *Endocr. Rev.* **43**, 984–1002 (2022).
10. Wan, M., Gray-Gaillard, E. F. & Elisseeff, J. H. Cellular senescence in musculoskeletal homeostasis, diseases, and regeneration. *Bone Res.* **9**, 41 (2021).
11. Kaur, J. & Farr, J. N. Cellular senescence in age-related disorders. *Transl. Res.* **226**, 96–104 (2020).
12. Gorgoulis, V. et al. Cellular senescence: defining a path forward. *Cell* **179**, 813–827 (2019).
13. Gurkar, A. U. et al. Spatial mapping of cellular senescence: emerging challenges and opportunities. *Nat. Aging* **3**, 776–790 (2023).
14. Gladyshev, V. N. et al. Molecular damage in aging. *Nat. Aging* **1**, 1096–1106 (2021).
15. Fang, C. L., Liu, B. & Wan, M. 'Bone-SASP' in skeletal aging. *Calcif. Tissue Int.* **113**, 68–82 (2023).
16. Khosla, S. et al. The role of cellular senescence in ageing and endocrine disease. *Nat. Rev. Endocrinol.* **16**, 263–275 (2020).
17. Ogrodnik, M. et al. Obesity-induced cellular senescence drives anxiety and impairs neurogenesis. *Cell Metab.* **29**, 1061–1077 (2019).
18. Jeon, O. H. et al. Systemic induction of senescence in young mice after single heterochronic blood exchange. *Nat. Metab.* **4**, 995–1006 (2022).
19. Liu, X. et al. Oxylipin-PPARγ-initiated adipocyte senescence propagates secondary senescence in the bone marrow. *Cell Metab.* **35**, 667–684 (2023).
20. Ambrosi, T. H. et al. Aged skeletal stem cells generate an inflammatory degenerative niche. *Nature* **597**, 256–262 (2021).
21. Zou, N. Y. et al. Age-related secretion of grancalcin by macrophages induces skeletal stem/progenitor cell senescence during fracture healing. *Bone Res.* **12**, 6 (2024).
22. Xu, M. et al. Transplanted senescent cells induce an osteoarthritis-like condition in mice. *J. Gerontol. A Biol. Sci. Med. Sci.* **72**, 780–785 (2017).
23. Li, C. J. et al. Senescent immune cells release grancalcin to promote skeletal aging. *Cell Metab.* **33**, 1957–1973 (2021).
24. Das, M. M. et al. Young bone marrow transplantation preserves learning and memory in old mice. *Commun Biol.* **2**, 73 (2019).
25. Inoue, A. et al. Young bone marrow transplantation prevents aging-related muscle atrophy in a senescence-accelerated mouse prone 10 model. *J. Cachexia Sarcopenia Muscle* **13**, 3078–3090 (2022).
26. Hurwitz, S. N., Jung, S. K. & Kurre, P. Hematopoietic stem and progenitor cell signaling in the niche. *Leukemia* **34**, 3136–3148 (2020).
27. Tikhonova, A. N. et al. The bone marrow microenvironment at single-cell resolution. *Nature* **569**, 222–228 (2019).
28. Comazzetto, S., Shen, B. & Morrison, S. J. Niches that regulate stem cells and hematopoiesis in adult bone marrow. *Dev. Cell* **56**, 1848–1860 (2021).
29. Welsh, J. A. et al. Minimal information for studies of extracellular vesicles (MISEV2023): from basic to advanced approaches. *J. Extracell. Vesicles* **13**, e12404 (2024).
30. Théry, C. et al. Minimal information for studies of extracellular vesicles 2018 (MISEV2018): a position statement of the International Society for Extracellular Vesicles and update of the MISEV2014 guidelines. *J. Extracell. Vesicles* **7**, 1535750 (2018).
31. Witwer, K. W. et al. Updating MISEV: evolving the minimal requirements for studies of extracellular vesicles. *J. Extracell. Vesicles* **10**, e12182 (2021).
32. Xu, D. & Tahara, H. The role of exosomes and microRNAs in senescence and aging. *Adv. Drug Deliv. Rev.* **65**, 368–375 (2013).
33. Kirkland, J. L. & Tchkonia, T. Senolytic drugs: from discovery to translation. *J. Intern. Med.* **288**, 518–536 (2020).
34. Grange, C. et al. Urinary extracellular vesicles carrying Klotho improve the recovery of renal function in an acute tubular injury model. *Mol. Ther.* **28**, 490–502 (2020).
35. Robbins, P. D., Dorronsoro, A. & Booker, C. N. Regulation of chronic inflammatory and immune processes by extracellular vesicles. *J. Clin. Invest.* **126**, 1173–1180 (2016).

36. Fafián-Labora, J. A. & O'Loghlen, A. Classical and nonclassical intercellular communication in senescence and ageing. *Trends Cell Biol.* **30**, 628–639 (2020).
37. Dorronsoro, A. et al. Mesenchymal stem cell-derived extracellular vesicles reduce senescence and extend health span in mouse models of aging. *Aging Cell* **20**, e13337 (2021).
38. Yin, Y. et al. Roles of extracellular vesicles in the aging microenvironment and age-related diseases. *J. Extracell. Vesicles* **10**, e12154 (2021).
39. Fafián-Labora, J. A., Rodríguez-Navarro, J. A. & O'Loghlen, A. Small extracellular vesicles have GST activity and ameliorate senescence-related tissue damage. *Cell Metab.* **32**, 71–86 (2020).
40. Chi, C. et al. Exerkine fibronectin type-III domain-containing protein 5/irisin-enriched extracellular vesicles delay vascular ageing by increasing SIRT6 stability. *Eur. Heart J.* **43**, 4579–4595 (2022).
41. Chen, X. et al. Small extracellular vesicles from young plasma reverse age-related functional declines by improving mitochondrial energy metabolism. *Nat. Aging* **4**, 814–838 (2024).
42. Zhang, Y. et al. Hypothalamic stem cells control ageing speed partly through exosomal miRNAs. *Nature* **548**, 52–57 (2017).
43. Zhang, X. et al. Rejuvenation of the aged brain immune cell landscape in mice through p16-positive senescent cell clearance. *Nat. Commun.* **13**, 5671 (2022).
44. Farr, J. N. et al. Local senolysis in aged mice only partially replicates the benefits of systemic senolysis. *J. Clin. Invest.* **133**, e162519 (2023).
45. Gasek, N. S. et al. Strategies for targeting senescent cells in human disease. *Nat. Aging* **1**, 870–879 (2021).
46. Farr, J. N. et al. Targeting cellular senescence prevents age-related bone loss in mice. *Nat. Med.* **23**, 1072–1079 (2017).
47. Wang, B. et al. An inducible *p21*-Cre mouse model to monitor and manipulate *p21*-highly-expressing senescent cells in vivo. *Nat. Aging* **1**, 962–973 (2021).
48. Palmer, A. K. et al. Targeting senescent cells alleviates obesity-induced metabolic dysfunction. *Aging Cell* **18**, e12950 (2019).
49. Wang, L. et al. Targeting $p21^{Cip1}$ highly expressing cells in adipose tissue alleviates insulin resistance in obesity. *Cell Metab.* **34**, 75–89 (2022).
50. Robbins, P. D. et al. Senolytic drugs: reducing senescent cell viability to extend health span. *Annu. Rev. Pharmacol. Toxicol.* **61**, 779–803 (2021).
51. Hickson, L. J. et al. Senolytics decrease senescent cells in humans: preliminary report from a clinical trial of Dasatinib plus Quercetin in individuals with diabetic kidney disease. *EBioMedicine* **47**, 446–456 (2019).
52. Xu, M. et al. JAK inhibition alleviates the cellular senescence-associated secretory phenotype and frailty in old age. *Proc. Natl Acad. Sci. USA* **112**, E6301–E6310 (2015).
53. Xu, M., Tchkonia, T. & Kirkland, J. L. Perspective: targeting the JAK/STAT pathway to fight age-related dysfunction. *Pharmacol. Res.* **111**, 152–154 (2016).
54. Zhu, Y. et al. The Achilles' heel of senescent cells: from transcriptome to senolytic drugs. *Aging Cell* **14**, 644–658 (2015).
55. Ma, S. et al. Heterochronic parabiosis induces stem cell revitalization and systemic rejuvenation across aged tissues. *Cell Stem Cell* **29**, 990–1005 (2022).
56. Jeon, O. H. et al. Senescence cell–associated extracellular vesicles serve as osteoarthritis disease and therapeutic markers. *JCI Insight* **4**, e125019 (2019).
57. Paumelle, R. et al. Hepatic PPARα is critical in the metabolic adaptation to sepsis. *J. Hepatol.* **70**, 963–973 (2019).
58. Pawlak, M., Lefebvre, P. & Staels, B. Molecular mechanism of PPARα action and its impact on lipid metabolism, inflammation and fibrosis in non-alcoholic fatty liver disease. *J. Hepatol.* **62**, 720–733 (2015).
59. Sun, N. et al. Hepatic Krüppel-like factor 16 (KLF16) targets PPARα to improve steatohepatitis and insulin resistance. *Gut* **70**, 2183–2195 (2021).
60. Khan, R. S. et al. Modulation of insulin resistance in nonalcoholic fatty liver disease. *Hepatology* **70**, 711–724 (2019).
61. Cai, Y. et al. Deficiency of telomere-associated repressor activator protein 1 precipitates cardiac aging in mice via p53/PPARα signaling. *Theranostics* **11**, 4710–4727 (2021).
62. Chung, K. W. et al. Impairment of PPARα and the fatty acid oxidation pathway aggravates renal fibrosis during aging. *J. Am. Soc. Nephrol.* **29**, 1223–1237 (2018).
63. Chiang, C. L. Introduction to stochastic processes in biostatistics. *J. Roy. Stat. Soc. D-Sta.* **19**, 77 (1969).
64. Su, W. et al. Senescent preosteoclast secretome promotes metabolic syndrome associated osteoarthritis through cyclooxygenase 2. *eLife* **11**, e79773 (2022).
65. Yousefzadeh, M. J. et al. An aged immune system drives senescence and ageing of solid organs. *Nature* **594**, 100–105 (2021).
66. Xu, M. et al. Senolytics improve physical function and increase lifespan in old age. *Nat. Med.* **24**, 1246–1256 (2018).
67. Castellano, J. M. et al. Human umbilical cord plasma proteins revitalize hippocampal function in aged mice. *Nature* **544**, 488–492 (2017).
68. Rebo, J. et al. A single heterochronic blood exchange reveals rapid inhibition of multiple tissues by old blood. *Nat. Commun.* **7**, 13363 (2016).
69. Villeda, S. A. et al. The ageing systemic milieu negatively regulates neurogenesis and cognitive function. *Nature* **477**, 90–94 (2011).
70. Yousef, H. et al. Aged blood impairs hippocampal neural precursor activity and activates microglia via brain endothelial cell VCAM1. *Nat. Med.* **25**, 988–1000 (2019).
71. Lau, A. et al. Mixing old and young: enhancing rejuvenation and accelerating aging. *J. Clin. Invest.* **129**, 4–11 (2019).
72. Bieri, G., Schroer, A. B. & Villeda, S. A. Blood-to-brain communication in aging and rejuvenation. *Nat. Neurosci.* **26**, 379–393 (2023).
73. Robbins, P. D. & Morelli, A. E. Regulation of immune responses by extracellular vesicles. *Nat. Rev. Immunol.* **14**, 195–208 (2014).
74. Zhang, H. et al. Circulating pro-inflammatory exosomes worsen stroke outcomes in aging. *Circ. Res.* **129**, e121–e140 (2021).
75. Lee, B. R. et al. Effect of young exosomes injected in aged mice. *Int. J. Nanomedicine* **13**, 5335–5345 (2018).
76. Sahu, A. et al. Regulation of aged skeletal muscle regeneration by circulating extracellular vesicles. *Nat. Aging* **1**, 1148–1161 (2021).
77. Xun, J. et al. Serum exosomes from young rats improve the reduced osteogenic differentiation of BMSCs in aged rats with osteoporosis after fatigue loading in vivo. *Stem Cell Res. Ther.* **12**, 424 (2021).
78. Lei, Q. et al. Extracellular vesicles deposit PCNA to rejuvenate aged bone marrow-derived mesenchymal stem cells and slow age-related degeneration. *Sci. Transl. Med.* **13**, eaaz8697 (2021).
79. Rather, H. A. et al. Therapeutic efficacy and promise of stem cell-derived extracellular vesicles in Alzheimer's disease and other aging-related disorders. *Ageing Res. Rev.* **92**, 102088 (2023).
80. Xiao, X. et al. Mesenchymal stem cell-derived small extracellular vesicles mitigate oxidative stress-induced senescence in endothelial cells via regulation of miR-146a/Src. *Signal Transduct. Target. Ther.* **6**, 354 (2021).
81. Iram, T. et al. Young CSF restores oligodendrogenesis and memory in aged mice via Fgf17. *Nature* **605**, 509–515 (2022).
82. Yousefzadeh, M. J. et al. Fisetin is a senotherapeutic that extends health and lifespan. *EBioMedicine* **36**, 18–28 (2018).

83. Zhou, Y. et al. Senolytics alleviate the degenerative disorders of temporomandibular joint in old age. *Aging Cell* **20**, e13394 (2021).
84. Zhou, Y. et al. Senolytics improve bone forming potential of bone marrow mesenchymal stem cells from aged mice. *npj Regen. Med.* **6**, 34 (2021).
85. Partridge, L., Fuentealba, M. & Kennedy, B. K. The quest to slow ageing through drug discovery. *Nat. Rev. Drug Discov.* **19**, 513–532 (2020).
86. Novais, E. J. et al. Long-term treatment with senolytic drugs Dasatinib and Quercetin ameliorates age-dependent intervertebral disc degeneration in mice. *Nat. Commun.* **12**, 5213 (2021).
87. Zhang, Y., Zhang, J. & Wang, S. The role of rapamycin in healthspan extension via the delay of organ aging. *Ageing Res. Rev.* **70**, 101376 (2021).
88. Justice, J. N. et al. Senolytics in idiopathic pulmonary fibrosis: results from a first-in-human, open-label, pilot study. *EBioMedicine* **40**, 554–563 (2019).
89. Kim, N. H. et al. Use of fenofibrate on cardiovascular outcomes in statin users with metabolic syndrome: propensity matched cohort study. *BMJ* **366**, l5125 (2019).
90. Jo, S. H. et al. Fenofibrate use is associated with lower mortality and fewer cardiovascular events in patients with diabetes: results of 10,114 patients from the Korean National Health Insurance Service Cohort. *Diabetes Care* **44**, 1868–1876 (2021).
91. Liu, W. et al. Hepatic miR-378 targets p110α and controls glucose and lipid homeostasis by modulating hepatic insulin signalling. *Nat. Commun.* **5**, 5684 (2014).
92. Kaur, S. et al. Self-repopulating recipient bone marrow resident macrophages promote long-term hematopoietic stem cell engraftment. *Blood* **132**, 735–749 (2018).
93. Ochi, K. et al. Non-conditioned bone marrow chimeric mouse generation using culture-based enrichment of hematopoietic stem and progenitor cells. *Nat. Commun.* **12**, 3568 (2021).
94. Xie, X. et al. Single-cell transcriptome profiling reveals neutrophil heterogeneity in homeostasis and infection. *Nat. Immunol.* **21**, 1119–1133 (2020).
95. Giladi, A. et al. Single-cell characterization of haematopoietic progenitors and their trajectories in homeostasis and perturbed haematopoiesis. *Nat. Cell Biol.* **20**, 836–846 (2018).
96. Pero, R. S. et al. $G\alpha_{i2}$-mediated signaling events in the endothelium are involved in controlling leukocyte extravasation. *Proc. Natl Acad. Sci. USA* **104**, 4371–4376 (2007).
97. Zhao, H. Y. et al. M2 macrophages, but not M1 macrophages, support megakaryopoiesis by upregulating PI3K-AKT pathway activity. *Signal Transduct. Target. Ther.* **6**, 234 (2021).
98. Poulos, M. G. et al. Endothelial transplantation rejuvenates aged hematopoietic stem cell function. *J. Clin. Invest.* **127**, 4163–4178 (2017).
99. Ying, W. et al. Adipose tissue macrophage-derived exosomal miRNAs can modulate in vivo and in vitro insulin sensitivity. *Cell* **171**, 372–384 (2017).
100. Liu, R. et al. Mechanosensitive protein polycystin-1 promotes periosteal stem/progenitor cells osteochondral differentiation in fracture healing. *Theranostics* **14**, 2544–2559 (2024).
101. Huang, M. et al. Mechanical protein polycystin-1 directly regulates osteoclastogenesis and bone resorption. *Sci. Bull. (Beijing)* **69**, 1964–1979 (2024).
102. Lewis, J. D. et al. Validation studies of the health improvement network (THIN) database for pharmacoepidemiology research. *Pharmacoepidemiol. Drug Saf.* **16**, 393–401 (2007).
103. American Diabetes Association Professional Practice Committee. 2. Classification and diagnosis of diabetes: Standards of Medical Care in Diabetes—2022. *Diabetes Care* **45**, S17–S38 (2022).
104. Zhao, S. S. et al. Improving rheumatoid arthritis comparative effectiveness research through causal inference principles: systematic review using a target trial emulation framework. *Ann. Rheum. Dis.* **79**, 883–890 (2020).
105. Hernán, M. A. & Robins, J. M. Using big data to emulate a target trial when a randomized trial is not available. *Am. J. Epidemiol.* **183**, 758–764 (2016).
106. Suissa, S., Moodie, E. E. & Dell'Aniello, S. Prevalent new-user cohort designs for comparative drug effect studies by time-conditional propensity scores. *Pharmacoepidemiol. Drug Saf.* **26**, 459–468 (2017).
107. Douros, A. et al. Sulfonylureas as second line drugs in type 2 diabetes and the risk of cardiovascular and hypoglycaemic events: population based cohort study. *BMJ* **362**, k2693 (2018).
108. Douros, A. et al. Sodium-glucose cotransporter-2 inhibitors and the risk for diabetic ketoacidosis: a multicenter cohort study. *Ann. Intern. Med.* **173**, 417–425 (2020).
109. Wright, A. K. et al. Life expectancy and cause-specific mortality in type 2 diabetes: a population-based cohort study quantifying relationships in ethnic subgroups. *Diabetes Care* **40**, 338–345 (2017).
110. Wei, J. et al. Lowering serum urate with urate-lowering therapy to target and incident fracture among people with gout. *Arthritis Rheumatol.* **75**, 1456–1465 (2023).
111. McGuinness, L. A. et al. The validity of dementia diagnoses in routinely collected electronic health records in the United Kingdom: a systematic review. *Pharmacoepidemiol. Drug Saf.* **28**, 244–255 (2019).
112. Austin, P. C. Optimal caliper widths for propensity-score matching when estimating differences in means and differences in proportions in observational studies. *Pharm. Stat.* **10**, 150–161 (2011).
113. Gooley, T. A. et al. Estimation of failure probabilities in the presence of competing risks: new representations of old estimators. *Stat. Med.* **18**, 695–706 (1999).

Acknowledgements

This work was funded with the following grants: National Key Research and Development Program of China (2022YFC3601900 to G.-H.L., 2022YFC3601905 to C.-J.L., 2022YFC3601903 to X.-H.L. and 2019YFA0111900 to Y.-Z.J); National Natural Science Foundation of China (82261160397, 82272560 and 81922017 to C.-J.L. and 82370891, 82170902 and 82270930 to X.-H.L.); Key Research and Development Program of Hunan Province (2022SK2023 to C.-J.L.); the Hunan Provincial Science and Technology Department (2023JJ30896 to C.-J.L.); the NSFC/RGC Joint Research Scheme; the Research Grants Council (UGC) of the Hong Kong Special Administrative Region; the National Natural Science Foundation of China (NSFC/RGC project no. N_CUHK483/22 to Y.-Z.J.); the Center for Neuromusculoskeletal Restorative Medicine (CNRM, inno@HK, to Y.-Z.J.); the Innovation and Technology Commission of Hong Kong SAR, China; the Science and Technology Innovation Program of Hunan Province (2023RC1027 to C.-J.L., 2022RC1009 to J.W. and 2022RC3075 to C.Z.); and Major Project of the Natural Science Foundation of Hunan Province (Open Competition) (grant no. 2021JC0002 to X.-H.L.) and the Central South University Research Programme of Advanced Interdisciplinary Studies (2023QYJC011 to C.-J.L.). The mouse illustrations in the figures were created using BioRender.

Author contributions

J.H., K.-X.C. and C.-J.L. conceived and designed the study and wrote the manuscript. C.H., M.H. and Y.-R.J. helped to collect samples. X.-X.L, J.W., C.Z. and G.-H.L. contributed to the population-based

cohort study. Q.-N.X., W.-Z.H., L.L., N.-Y.Z., M.H., Y.X. and M.Y. contributed to the materials. C.-J.L., C.Z., G.-H.L., X.-H.L. and Y.-Z.J. made valuable suggestions regarding this study and co-supervised the writing of the paper. C.Z., G.-H.L. and C.-J.L. directed and supervised the study. All authors contributed to the manuscript and approved the submitted version.

Competing interests
The authors declare no competing interests.

Additional information
Extended data is available for this paper at https://doi.org/10.1038/s43587-024-00694-0.

Supplementary information The online version contains supplementary material available at https://doi.org/10.1038/s43587-024-00694-0.

Correspondence and requests for materials should be addressed to Chao Zeng, Guang-Hua Lei or Chang-Jun Li.

Peer review information *Nature Aging* thanks the anonymous reviewers for their contribution to the peer review of this work.

Reprints and permissions information is available at www.nature.com/reprints.

Publisher's note Springer Nature remains neutral with regard to jurisdictional claims in published maps and institutional affiliations.

[1]Department of Endocrinology, Endocrinology Research Center, Xiangya Hospital of Central South University, Changsha, China. [2]Hunan Key Laboratory of Joint Degeneration and Injury, Changsha, China. [3]Key Laboratory of Aging-related Bone and Joint Diseases Prevention and Treatment, Ministry of Education, Xiangya Hospital, Central South University, Changsha, China. [4]School of Biomedical Sciences, Institute for Tissue Engineering and Regenerative Medicine, Faculty of Medicine, Chinese University of Hong Kong, Hong Kong, China. [5]Center for Neuromusculoskeletal Restorative Medicine, Hong Kong Special Administrative Region of China, Hong Kong, China. [6]Department of Orthopaedics, Xiangya Hospital of Central South University, Changsha, China. [7]Department of Epidemiology and Health Statistics, Xiangya School of Public Health, Central South University, Changsha, China. [8]National Clinical Research Center for Geriatric Disorders, Xiangya Hospital, Central South University, Changsha, China. [9]Laboratory Animal Center, Xiangya Hospital, Central South University, Changsha, China. [10]These authors contributed equally: Jing Hou, Kai-Xuan Chen. ✉e-mail: zengchao@csu.edu.cn; lei_guanghua@csu.edu.cn; lichangjun@csu.edu.cn

https://doi.org/10.1038/s43587-024-00694-0

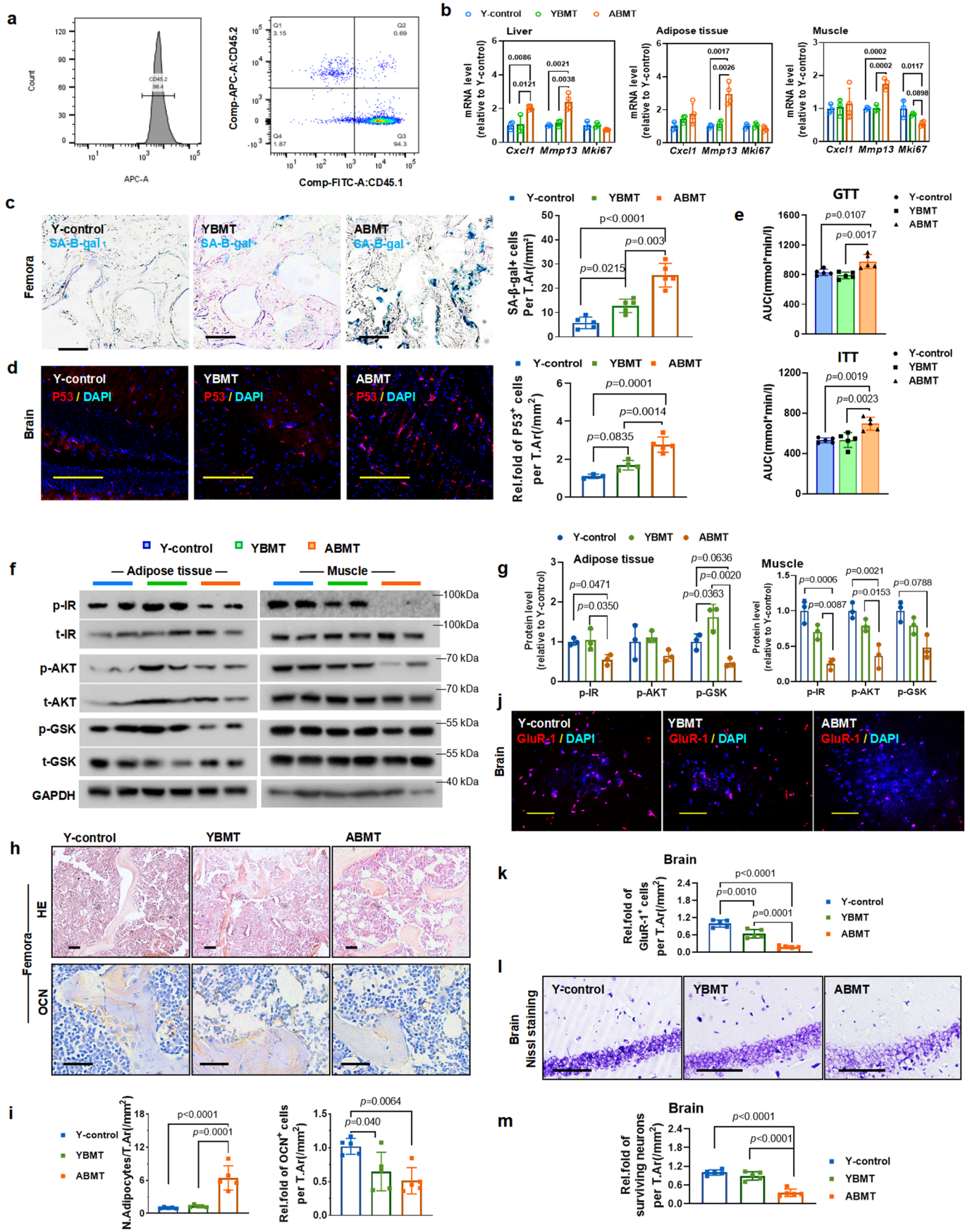

Extended Data Fig. 1 | See next page for caption.

https://doi.org/10.1038/s43587-024-00694-0

Extended Data Fig. 1 | Aged bone marrow drives senescence in young recipients. a, CD45.2 expression in white blood cells (enriched from total blood cells by red blood cell lysis) of CD45.2 recipient mice before irradiation, and CD45.1 and CD45.2 expression in white blood cells after transplantation of CD45.1 donor bone marrow cells ($n = 3$ mice). **b**, Expression of senescence-related genes in liver, muscle and adipose tissue of young recipients after bone marrow transplantation ($n = 4$ mice for ABMT; $n = 3$ mice for other groups). **c**, Representative SA-β-gal staining in femoral bone sections (scale bar, 50μm; $n = 5$ mice; 5 ~ 6 images per mouse). **d**, Representative p53 fluorescence image in brain (scale bar, 50μm; $n = 5$ mice for ABMT; $n = 4$ mice for other groups; 5 ~ 6 images per mouse). **e**, The AUC data for GTT and ITT were calculated, respectively ($n = 5$ mice). **f-g**, Western blot analysis of key molecules of insulin pathway in muscle and adipose tissue, and their quantitative data ($n = 3$ mice). **h-i**, Representative HE staining and osteocalcin staining in femoral bone sections (scale bar, 50μm; $n = 5$ mice; 5 ~ 6 images per mouse), and their quantitative data. **j-k**, Immunofluorescence for GluR-1 protein in brain and quantitative analysis (scale bar, 50μm; $n = 5$ mice; 5 ~ 6 images per mouse). **l-m**, Nissl staining in brain and quantitative analysis (scale bar, 50μm; $n = 5$ mice; 5 ~ 6 images per mouse). Data are presented as mean ± SEM. *P < 0.05; **P < 0.01; ***P < 0.001; #P < 0.0001, as determined by one-way ANOVA followed by Tukey's multiple comparison test.

https://doi.org/10.1038/s43587-024-00694-0

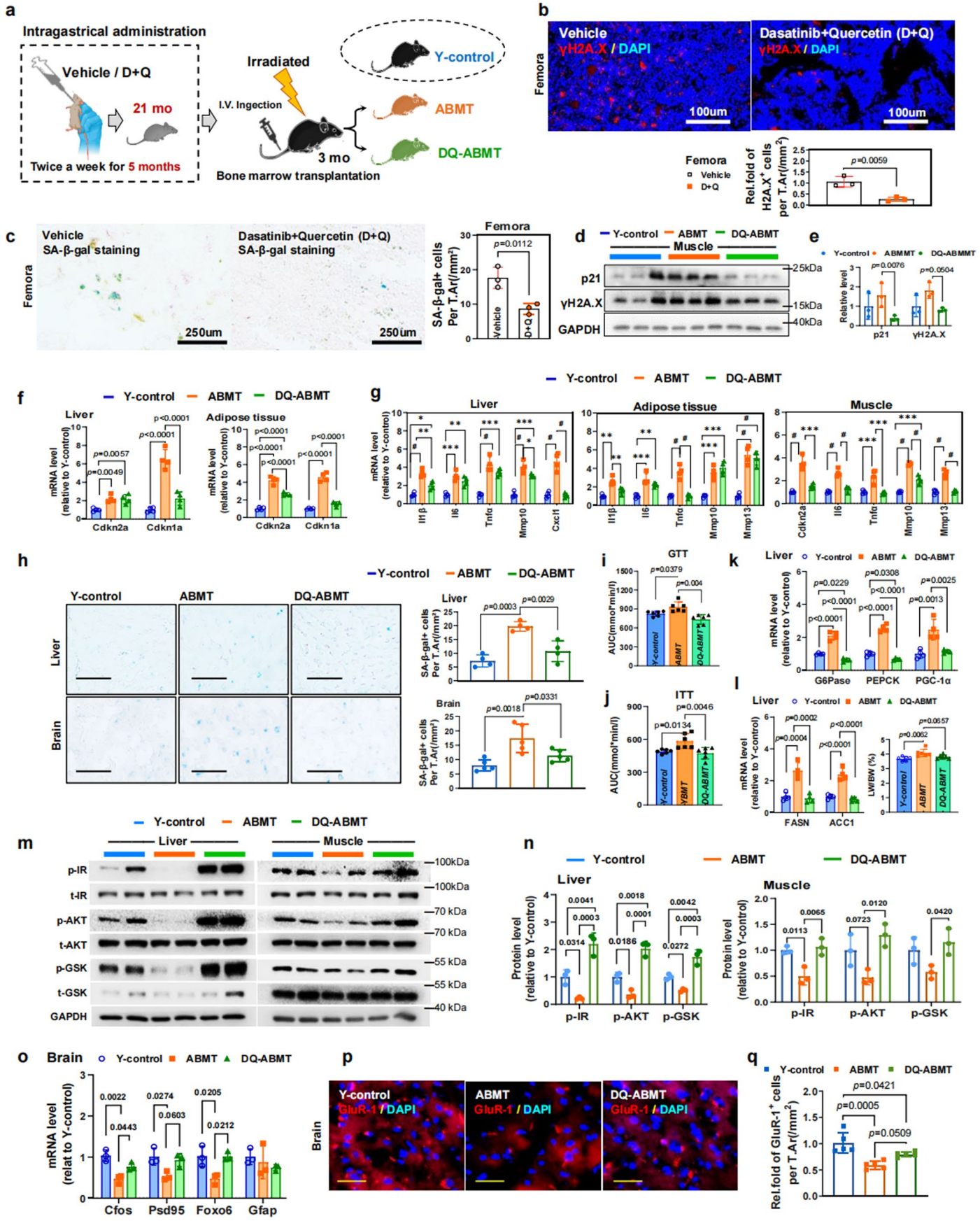

Extended Data Fig. 2 | See next page for caption.

https://doi.org/10.1038/s43587-024-00694-0

Extended Data Fig. 2 | Senolytics blunt the ability of aged bone marrow to induce senescence propagation to young recipients. a, Outline of the studies (male mice). Old mice (16 m, male) were treated with Vehicle or D + Q for 5months. After 5 months, bone marrow was isolated from mice and then transplanted into young mice (3 m, male) (ABMT, DQ-ABMT). **b**, Immunofluorescence staining of γH2A.X in femoral bone sections (scale bar, 100μm; *n* = 3 mice; 5 ~ 6 images per mouse). **c**, Representative SA-β-gal staining of bone marrow in aged mice after DQ administration (scale bar, 250μm; *n* = 3 mice; 5 ~ 6 images per mouse). **d-e**, The protein levels of senescence-associated markers in muscle and quantitative analysis (*n* = 3 mice). **f-g**, Gene expression of senescence-associated markers in liver, muscle and adipose tissue of young mice receiving bone marrow from DQ-treated aged mice (*n* = 4 mice). **h**, Representative images of SA-β-gal staining in the liver (scale bar, 50μm; *n* = 4 mice; 5 ~ 6 images per mouse) and brain (scale bar, 50μm; *n* = 5 mice; 5 ~ 6 images per mouse). **i-j**, The AUC data for GTT and ITT were calculated, respectively (*n* = 6 mice). **k**, The mRNA levels of G6Pase, PEPCK, and PGC-1a in the liver (*n* = 4 mice). **l**, Gene expression of FASN and ACC1 in liver (*n* = 4 mice), and the LW/BW of young recipients (*n* = 6 mice). **m-n**, Western blot analysis of phosphorylated key molecules of insulin pathway in the liver and muscle, and their quantitative data (*n* = 3 mice). **o**, The mRNA levels of C-fos, Psd95, Foxo6 and Gfap in the brain (*n* = 3 mice). **p-q**, Immunofluorescence detection of GluR-1 in the brain and quantitative analysis (scale bar, 50μm; *n* = 5 mice; 5 ~ 6 images per mouse). Data are presented as mean ± SEM. *P < 0.05; **P < 0.01, ***P < 0.001; #P < 0.0001 were determined using two-tailed *t*-test in **b-c** and one-way ANOVA followed by Tukey's multiple comparison test in **d-q**.

https://doi.org/10.1038/s43587-024-00694-0

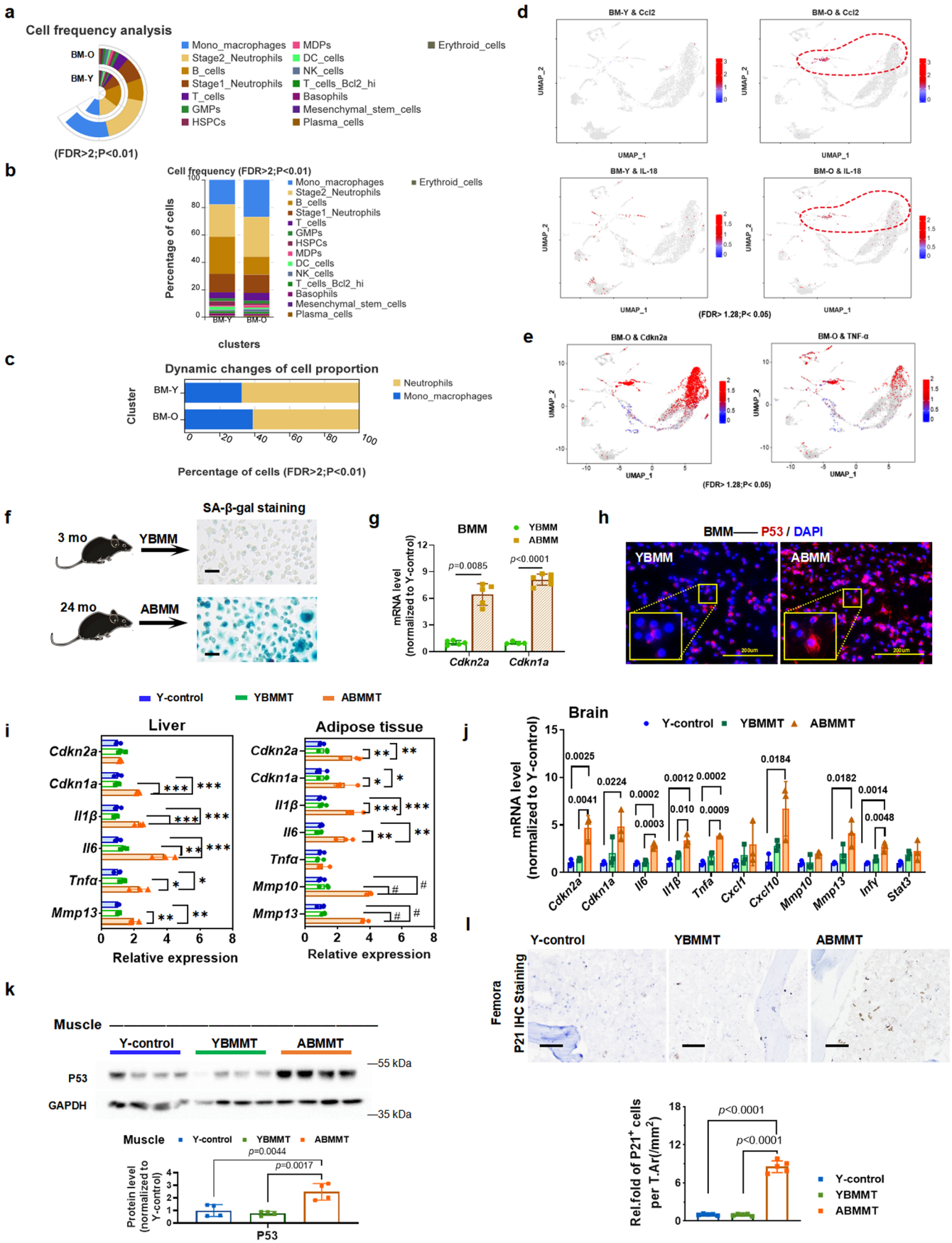

Extended Data Fig. 3 | See next page for caption.

https://doi.org/10.1038/s43587-024-00694-0

Extended Data Fig. 3 | Bone marrow monocytes/macrophages are more susceptible to senescence during aging. a-b, The number of cells and the percentage of cells are displayed by cell frequency analysis. **c**, Dynamic changes of cell proportion in BMMs and neutrophils. **d**, UMAP plots show the distribution of senescence-related genes in different cell types in young and old bone marrow (BM-Y, BM-O). **e**, UMAP plots show the expression and distribution of senescence-related genes in old bone marrow cells (BM-O). **f**, SA-β-gal staining in BMMs isolated from young (3 m, *n* = 3 male mice) and aged mice (24 m, *n* = 3 male mice), respectively (scale bar, 50μm). **g**, The expression levels of senescence-related genes in BMMs (*n* = 3 mice). **h**, p53 immunofluorescence staining in BMMs (scale bar, 200μm; *n* = 3 mice; 5 ~ 6 images per *n*). **i-j**, Expression levels of senescence markers in liver, adipose tissue and brain of young mice after BMMs transplantation (*n* = 3 mice). **k**, Western blot analysis of p53 protein expression in muscle (*n* = 4 mice). **l**, Representative images of p21 immunohistochemistry in femur (scale bar, 50μm; *n* = 5 mice; 5 ~ 6 images per mouse). Mean ± SEM are shown for all panels. *P < 0.05; **P < 0.01; ***P < 0.001; #P < 0.0001 were determined using two-tailed *t*-test in **a-f**, **g** (Cdkn1a) and **h**, two-tailed *t*-test with a Welch's correction in **g** (Cdkn2a) and one-way ANOVA followed by Tukey's multiple comparison test in **i-l**.

https://doi.org/10.1038/s43587-024-00694-0

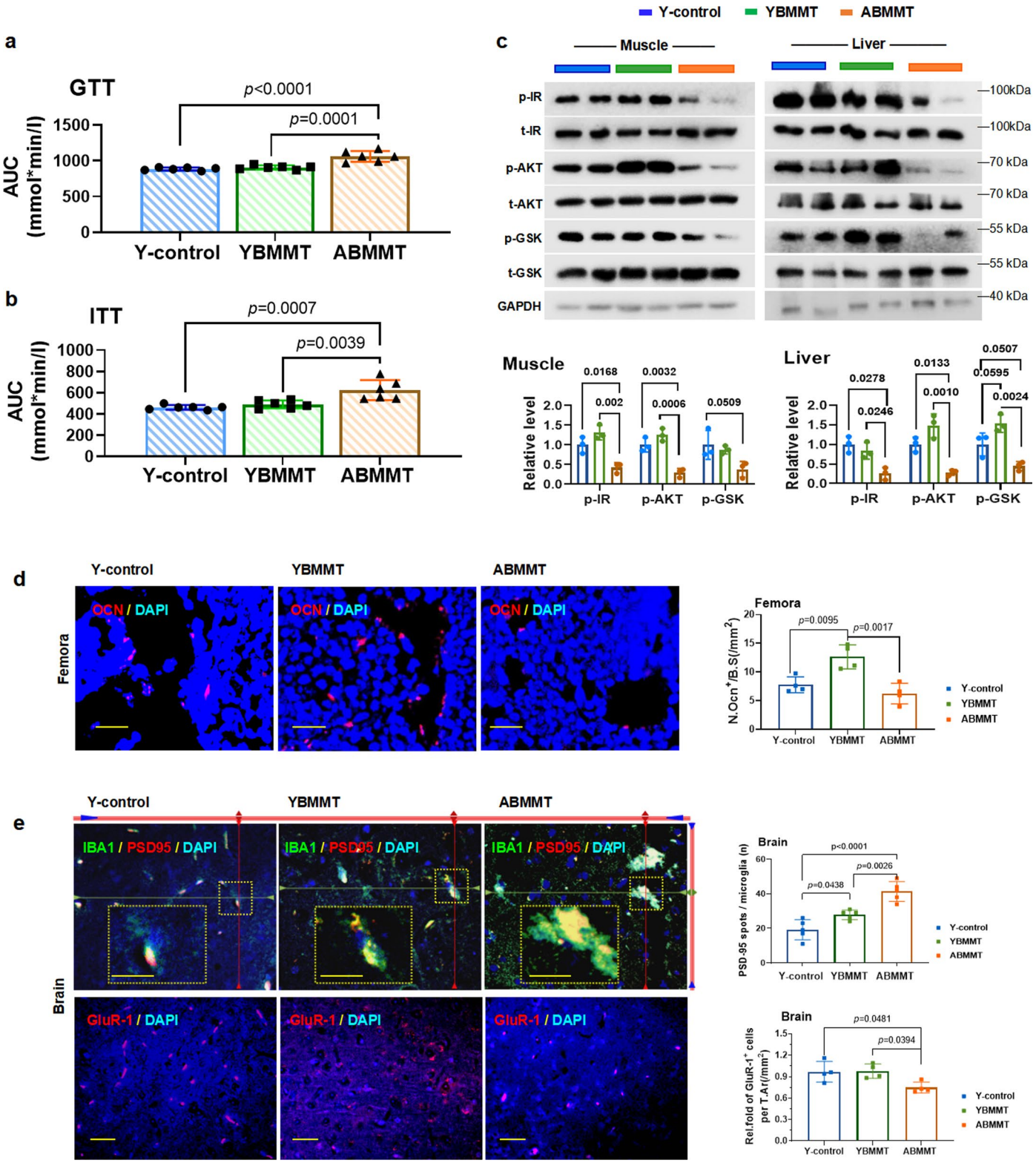

Extended Data Fig. 4 | Senescent BMMs lead to the propagation of senescent phenotypes to young murine. a-b, AUC data for GTT and ITT were calculated, respectively ($n = 6$ mice). **c**, Western blot analysis of key molecules in the insulin signaling pathway in liver and muscle ($n = 3$ mice). **d**, Osteocalcin staining was performed in femoral bone sections after BMMs transplantation (scale bar, 50μm; $n = 4$ mice; 5 - 6 images per mouse). **e**, Representative images and quantification of the number of PSD95+ synapses that engulfed by microglia (scale bar, 50μm; $n = 5$ mice; 5 - 6 images per mouse) and immunofluorescence detection of GluR-1 in brain (scale bar, 50μm; $n = 4$ mice; 5 - 6 images per mouse). Mean ± SEM are shown for all panels. *P < 0.05; **P < 0.01; ***P < 0.001; #P < 0.0001 according to one-way ANOVA followed by Tukey's multiple comparison test.

https://doi.org/10.1038/s43587-024-00694-0

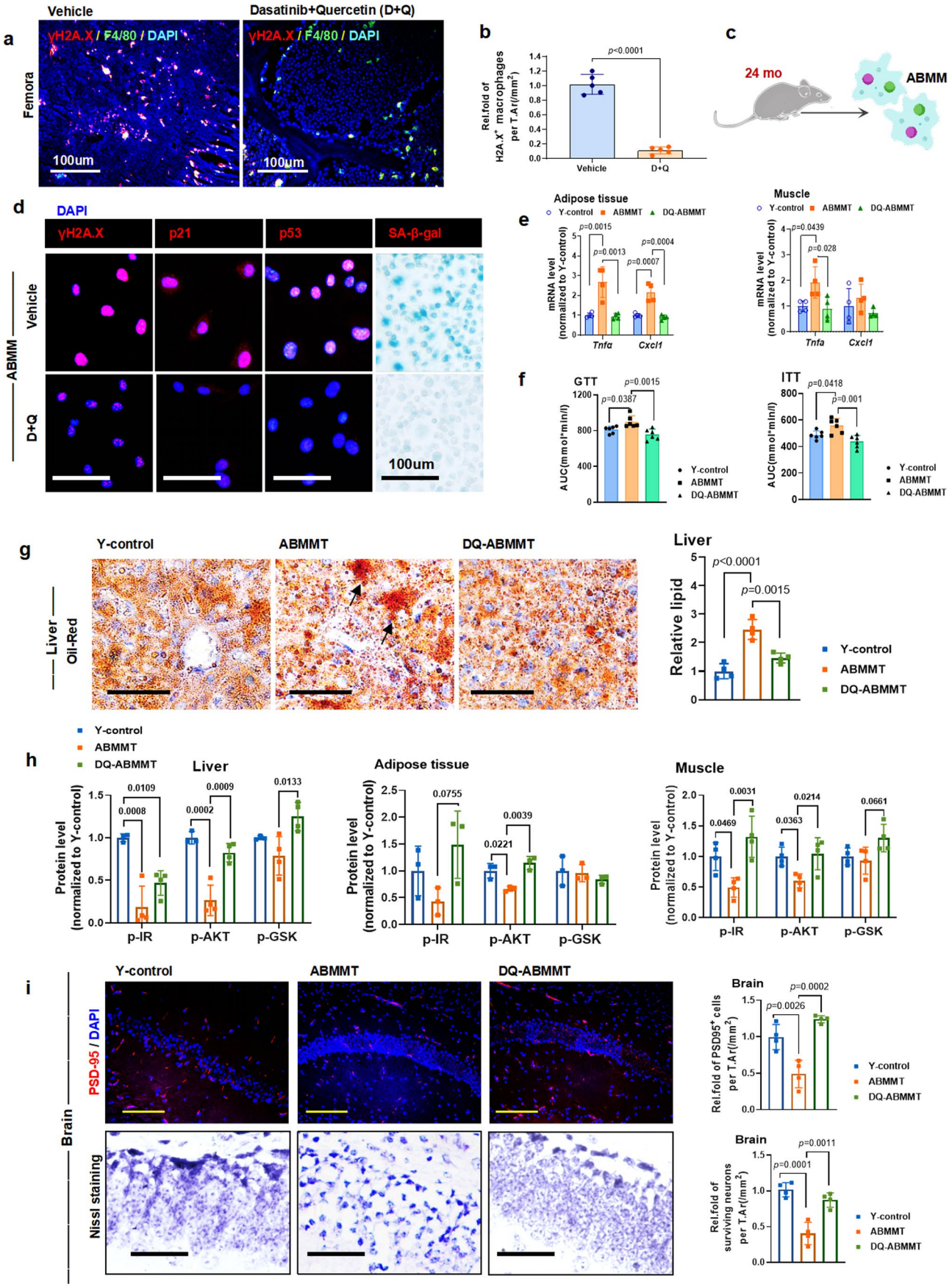

Extended Data Fig. 5 | See next page for caption.

https://doi.org/10.1038/s43587-024-00694-0

Extended Data Fig. 5 | Senolytics can eliminate senescent BMMs, and alleviate their pro-aging effects on multiple young tissues. a-b, Representative images (scale bar, 100μm; *n* = 5 mice; 5 ~ 6 images per mouse) and quantification of the number of γH2A.X+ macrophage in bone marrow after *in vivo* DQ treatment. **c-d**, SA-β-gal staining and immunofluorescence staining of p21, γH2A.X and p53 in BMMs after *in vitro* DQ treatment (scale bar, 100μm; *n* = 3 mice; 5 ~ 6 images per *n*). **e**, Expression levels of SASP factors in muscle and adipose tissue of young mice transplanted with DQ-treated BMMs (*n* = 4 mice). **f**, The AUC data for GTT and ITT were calculated, respectively (*n* = 6 mice). **g**, Representative liver Oil-Red staining (scale bar, 50μm; *n* = 4 mice; 5 ~ 6 images per mouse). **h**, Quantification of phosphorylation levels of insulin signaling in liver (*n* = 3 mice for Y-control; *n* = 4 mice for other groups), muscle (*n* = 4 mice) and adipose tissue (*n* = 3 mice). **i**, Representative images of PSD95 immunofluorescence and Nissl staining in brain (scale bar, 50μm; *n* = 4 mice; 5 ~ 6 images per mouse). Data are presented as mean ± SEM. *P < 0.05; **P < 0.01; ***P < 0.001; #P < 0.0001 were determined using two-tailed *t*-test in **a-d** and one-way ANOVA followed by Tukey's multiple comparison test in **e-i**.

https://doi.org/10.1038/s43587-024-00694-0

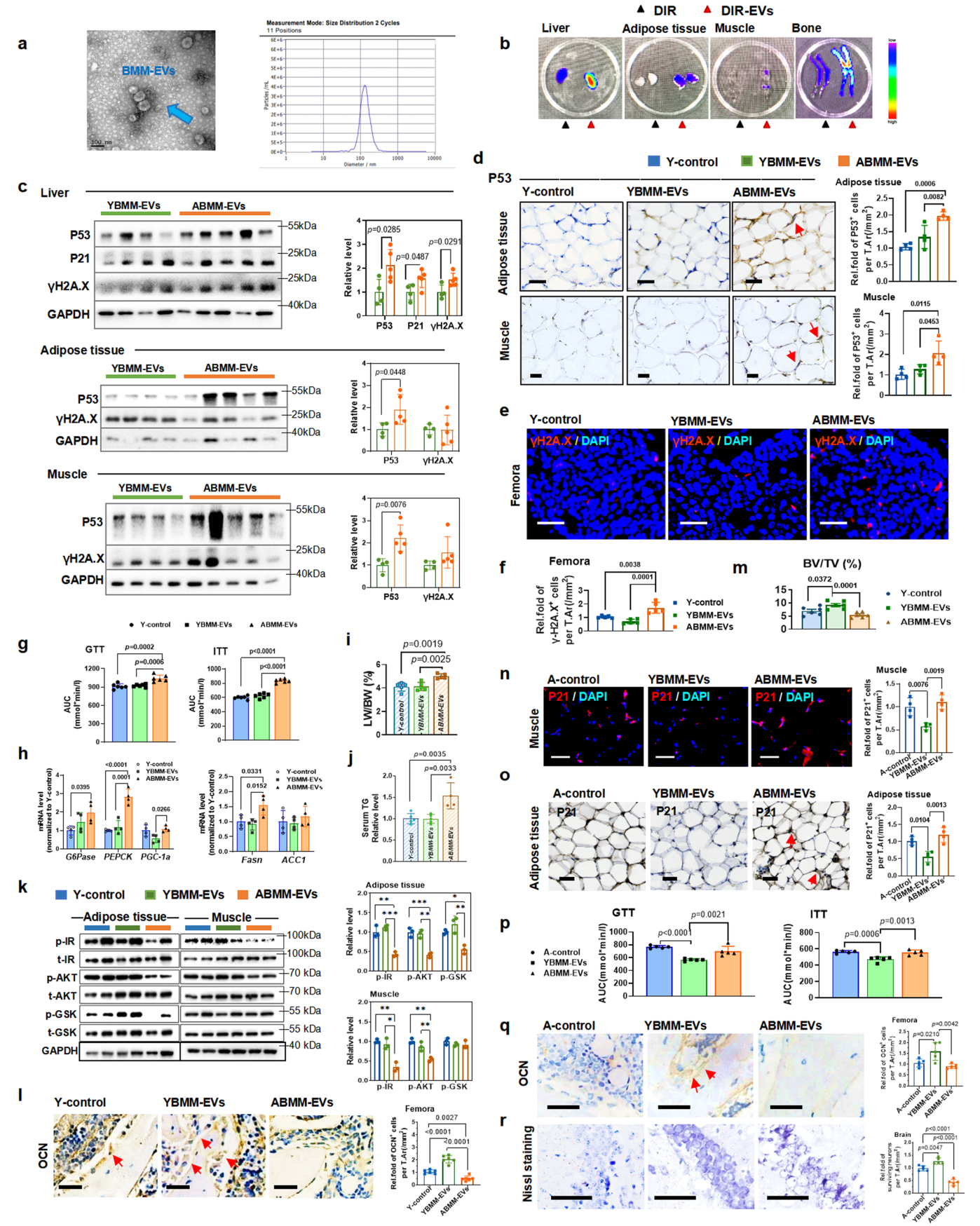

Extended Data Fig. 6 | See next page for caption.

https://doi.org/10.1038/s43587-024-00694-0

Extended Data Fig. 6 | EVs secreted by senescent BMMs propagate senescence, whereas young BMM-derived EVs ameliorate aging-related phenotypes of aged mice. a, The electron microscopy analysis (scale bar, 100 nm) and particle size of EVs ($n = 3$ mice). **b**, The uptake of EVs by multiple tissues ($n = 3$ mice). **c**, Protein levels of senescence markers in multiple tissues of young mice treated with YBMM-EVs or ABMM-EVs ($n = 4$ mice for YBMM-EVs; $n = 5$ mice for ABMM-EVs). **d**, Immunohistochemical staining of p53 in muscle and adipose tissue (scale bar, 50μm; $n = 4$ mice). **e-f**, Immunofluorescence staining for γH2A.X in bone sections, and the quantitative analysis (scale bar, 50μm; $n = 5$ mice). **g**, AUC data of GTT and ITT were calculated respectively ($n = 6$ mice). **h**, Expression levels of G6Pase, PEPCK, PGC-1a, FASN and ACC1 in the liver ($n = 4$ mice). **i**, The LW/BW were measured in young recipients ($n = 5$ mice). **j**, Serum triglyceride (TG) levels ($n = 5$ mice for Y-control and YBMM-EVs; $n = 4$ mice for ABMM-EVs). **k**, Phosphorylation levels of insulin signaling in muscle and adipose tissue ($n = 3$ mice). **l**, Osteocalcin immunohistochemical staining of femoral bone sections (scale bar, 50μm; $n = 6$ mice). **m**, Quantitative analysis of trabecular bone related parameters (BV/TV) ($n = 6$ mice). **n**, Immunofluorescence detection of p21 in muscle of aged mice after treatment with YBMM-EVs or ABMM-EVs (scale bar, 50μm; $n = 4$ mice; 5 ~ 6 images per mouse). **o**, Representative images of p21 immunohistochemistry in adipose tissue (scale bar, 50μm; $n = 4$ mice). **p**, The AUC data of GTT and ITT ($n = 5$ mice). **q**, Immunohistochemical staining of osteocalcin in femurs (scale bar, 50μm; $n = 5$ mice). **r**, Nissl staining in brain (scale bar, 50μm; $n = 5$ mice; 5 ~ 6 images per mouse). Data are expressed as mean ± SEM. *P < 0.05; **P < 0.01; ***P < 0.001; #P < 0.0001 were determined using two-tailed *t*-test in **c**. and one-way ANOVA followed by Tukey's multiple comparison test in **d-r**.

https://doi.org/10.1038/s43587-024-00694-0

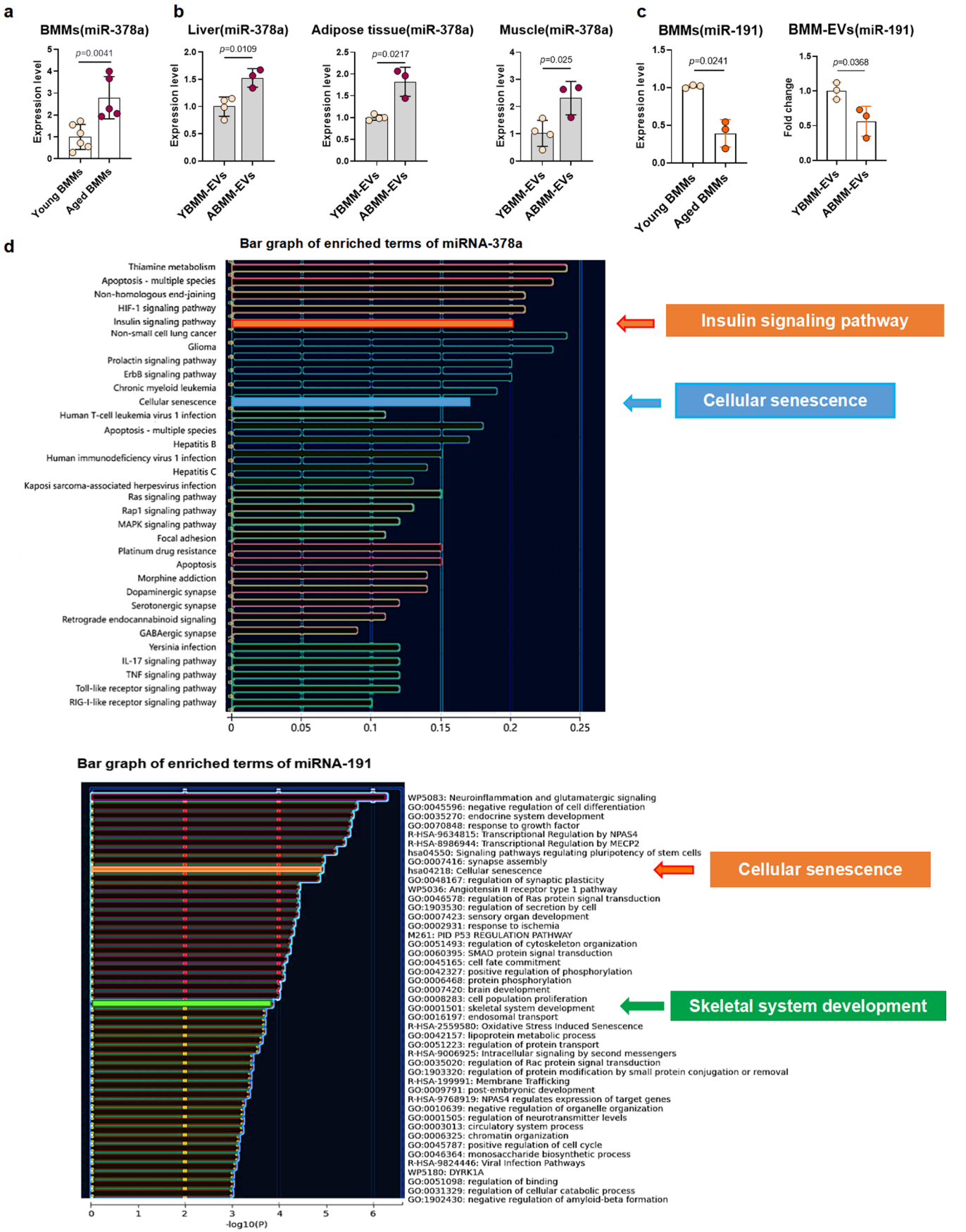

Extended Data Fig. 7 | See next page for caption.

https://doi.org/10.1038/s43587-024-00694-0

Extended Data Fig. 7 | BMMs-EVs containing miRNAs enrichment pathways. **a**, Expression level of miRNA-378a in BMMs isolated from young (3 m, male mice) and aged mice (24 m, male mice) ($n = 6$ young mice; $n = 5$ aged mice). **b**, Expression level of miRNA-378a in liver, adipose tissues and muscle of young mice after YBMM-EVs or ABMM-EVs treatment ($n = 4$ mice for YBMM-EVs; $n = 3$ mice for ABMM-EVs). **c**, Expression level of miRNA-191 in BMMs and their derived EVs ($n = 3$ mice). **d**, Bar plots of enriched terms of miR-378a and miR-191. Data are shown as mean ± SEM. *P < 0.05; **P < 0.01were determined using two-tailed *t*-test in **a**, **b** (liver and muscle) and **c** (BMM-EVs) and two-tailed *t*-test with a Welch's correction in **b** (adipose tissues) and **c** (BMMs).

https://doi.org/10.1038/s43587-024-00694-0

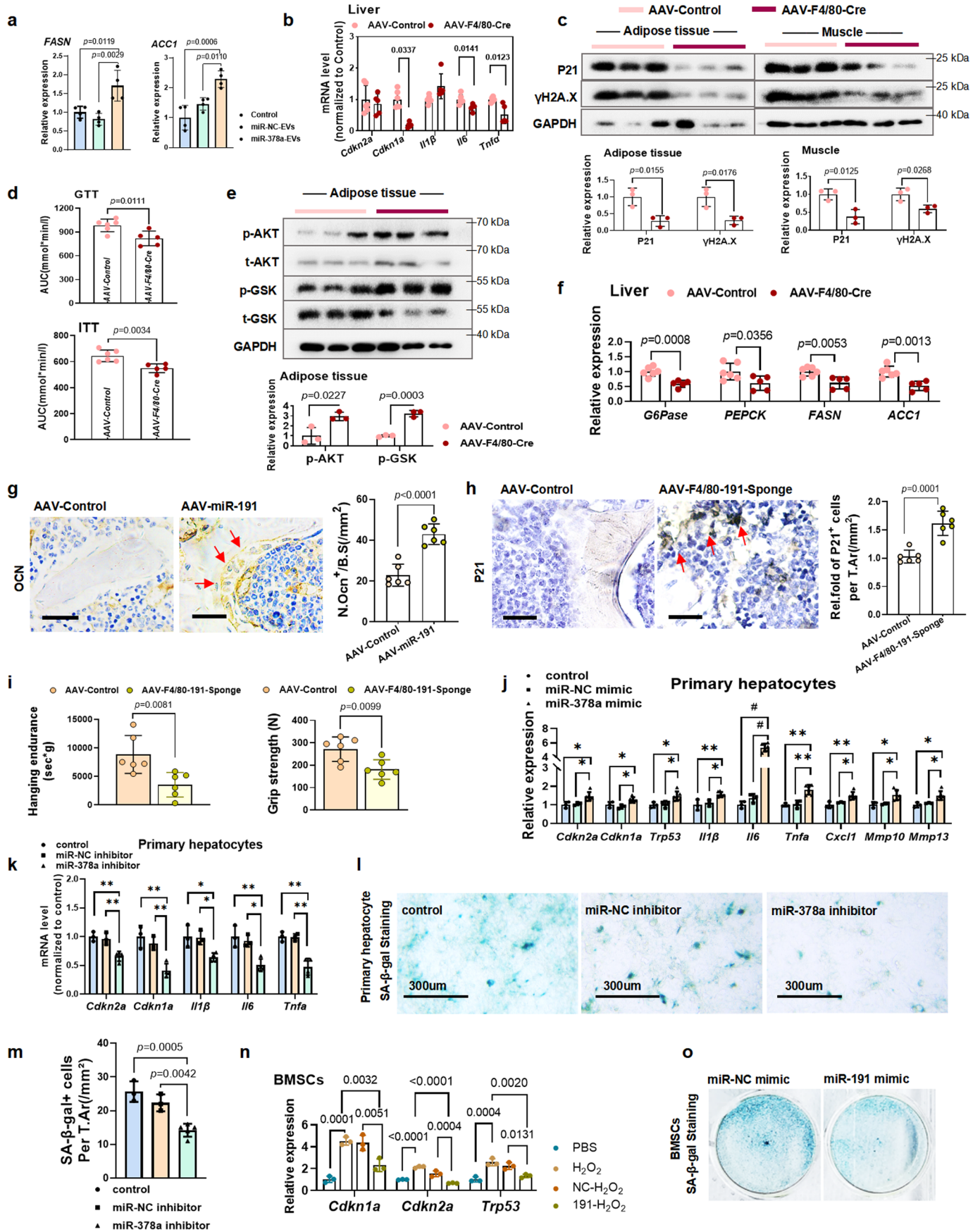

Extended Data Fig. 8 | See next page for caption.

https://doi.org/10.1038/s43587-024-00694-0

Extended Data Fig. 8 | MiR-378a and miR-191 regulate age-related dysfunction. a, The mRNA levels of FASN and ACC1 in liver of young recipients transplanted with macrophage-miR-378a-EVs ($n = 4$ mice). **b**, The mRNA levels of senescence-related markers in liver ($n = 6$ mice for AAV-Control; $n = 5$ mice for AAV-F4/80-Cre). **c**, Protein levels of senescence markers in muscle and adipose tissue of miR-378a-BMM-CKO mice ($n = 3$ mice). **d**, The AUC data of GTT and ITT ($n = 6$ mice for AAV-Control; $n = 5$ mice for AAV-F4/80-Cre). **e**, Phosphorylation levels of insulin signaling in adipose tissue ($n = 3$ mice). **f**, Expression levels of G6Pase, PEPCK, FASN and ACC1 in the liver ($n = 6$ mice for AAV-Control; $n = 5$ mice for AAV-F4/80-Cre). **g**, Immunohistochemical staining of osteocalcin in femurs of aged mice injected with AAV-miR-191 (scale bar, 50μm; $n = 6$ mice). **h**, Immunohistochemical staining of p21 in femurs of young mice injected with AAV-F4/80-miR-191-sponge (scale bar, 50μm; $n = 6$ mice). **i**, Hanging endurance and grip strength ($n = 6$ mice). **j**, The mRNA levels of senescence-related markers in primary hepatocytes after miR-378a overexpression ($n = 6$ biological replicates for miR-378a mimic; $n = 3$ biological replicates for other groups). **k**, The mRNA levels of senescence-related markers in primary hepatocytes after inhibition of miR-378a expression ($n = 4$ biological replicates for miR-378a inhibitor; $n = 3$ biological replicates for other groups). **l-m**, Representative images of SA-β-gal staining in primary hepatocytes (scale bar, 300μm; $n = 5$ biological replicates for miR-378a inhibitor; $n = 3$ biological replicates for other groups), and their quantitative data. **n**, The mRNA levels of senescence-related markers in BMSCs after miR-191 overexpression ($n = 3$ biological replicates). **o**, Representative images of SA-β-gal staining in BMSCs ($n = 3$ biological replicates). Data are shown as mean ± SEM. *P < 0.05; **P < 0.01; ***P < 0.001; #P < 0.0001 were determined using two-tailed *t*-test in **b** (Cdkn2a, Il-1β and Il-6), **c-i** and **o**, two-tailed *t*-test with a Welch's correction in **b** (Cdkn1a and Tnf-α) and one-way ANOVA followed by Tukey's multiple comparison test in **a**, **j-n**.

https://doi.org/10.1038/s43587-024-00694-0

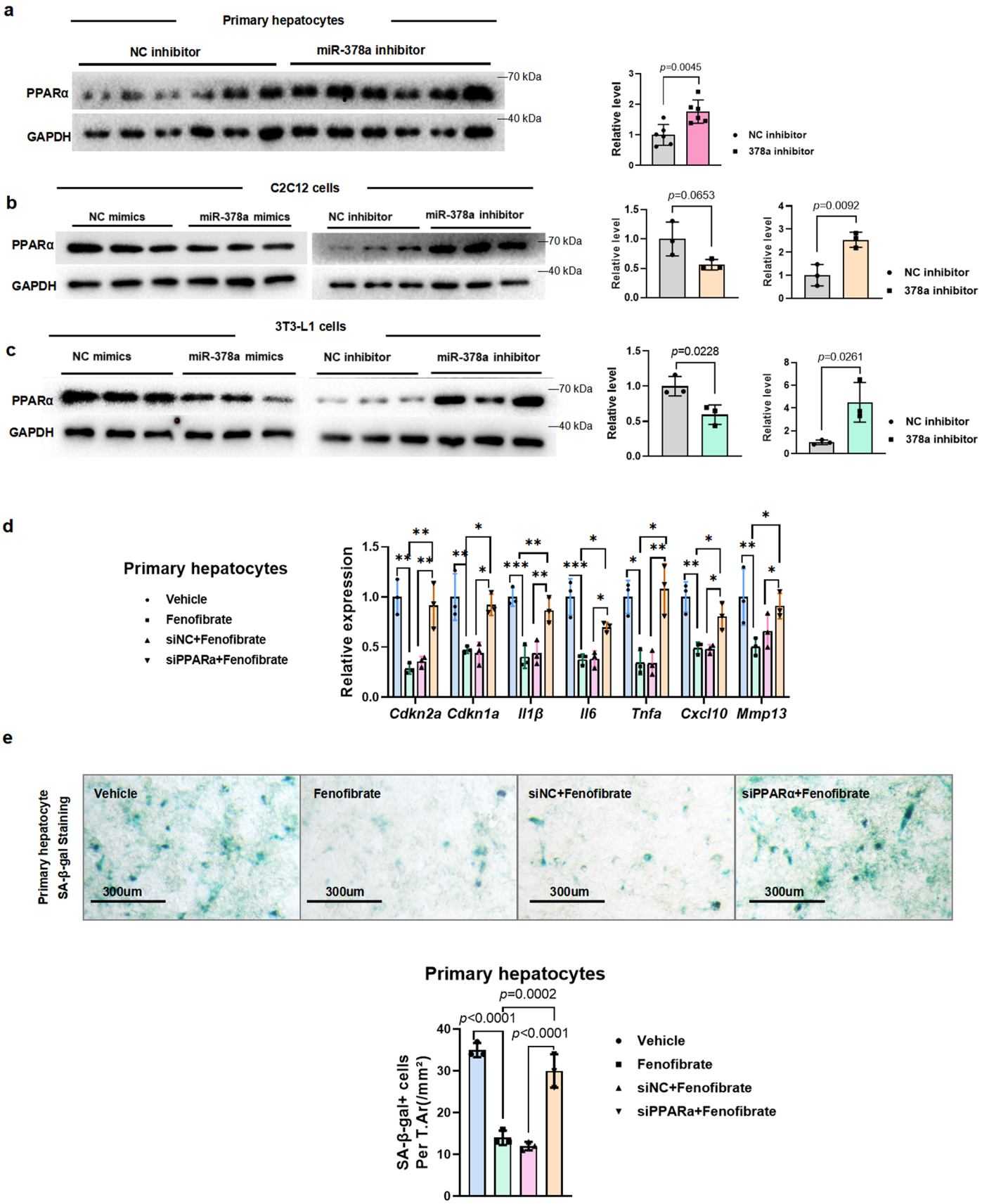

Extended Data Fig. 9 | See next page for caption.

https://doi.org/10.1038/s43587-024-00694-0

Extended Data Fig. 9 | Fenofibrate regulates cellular senescence by targeting PPARα. a, Protein levels of PPARα after inhibition of miRNA-378a expression in primary hepatocytes ($n = 6$ biological replicates). **b-c**, Protein levels of PPARα after overexpression or inhibition of miRNA-378a in C2C12 cells ($n = 3$ biological replicates) and 3T3-L1 cells ($n = 3$ biological replicates). **d**, Effects of Fenofibrate supplementation on mRNA levels of senescence-related markers in primary hepatocytes after inhibition of PPARα expression ($n = 3$ biological replicates). **e**, Representative images of SA-β-gal staining in primary hepatocytes (scale bar, 300μm; $n = 3$ biological replicates; 5 - 6 images per n). Data are expressed as mean ± SEM. *P < 0.05; **P < 0.01; ***P < 0.001; #P < 0.0001 were determined using two-tailed t-test in **a-b**, and **c** (mimic), two-tailed t-test with a Welch's correction in **c** (inhibitor) and one-way ANOVA followed by Tukey's multiple comparison test in **d-e**.

https://doi.org/10.1038/s43587-024-00694-0

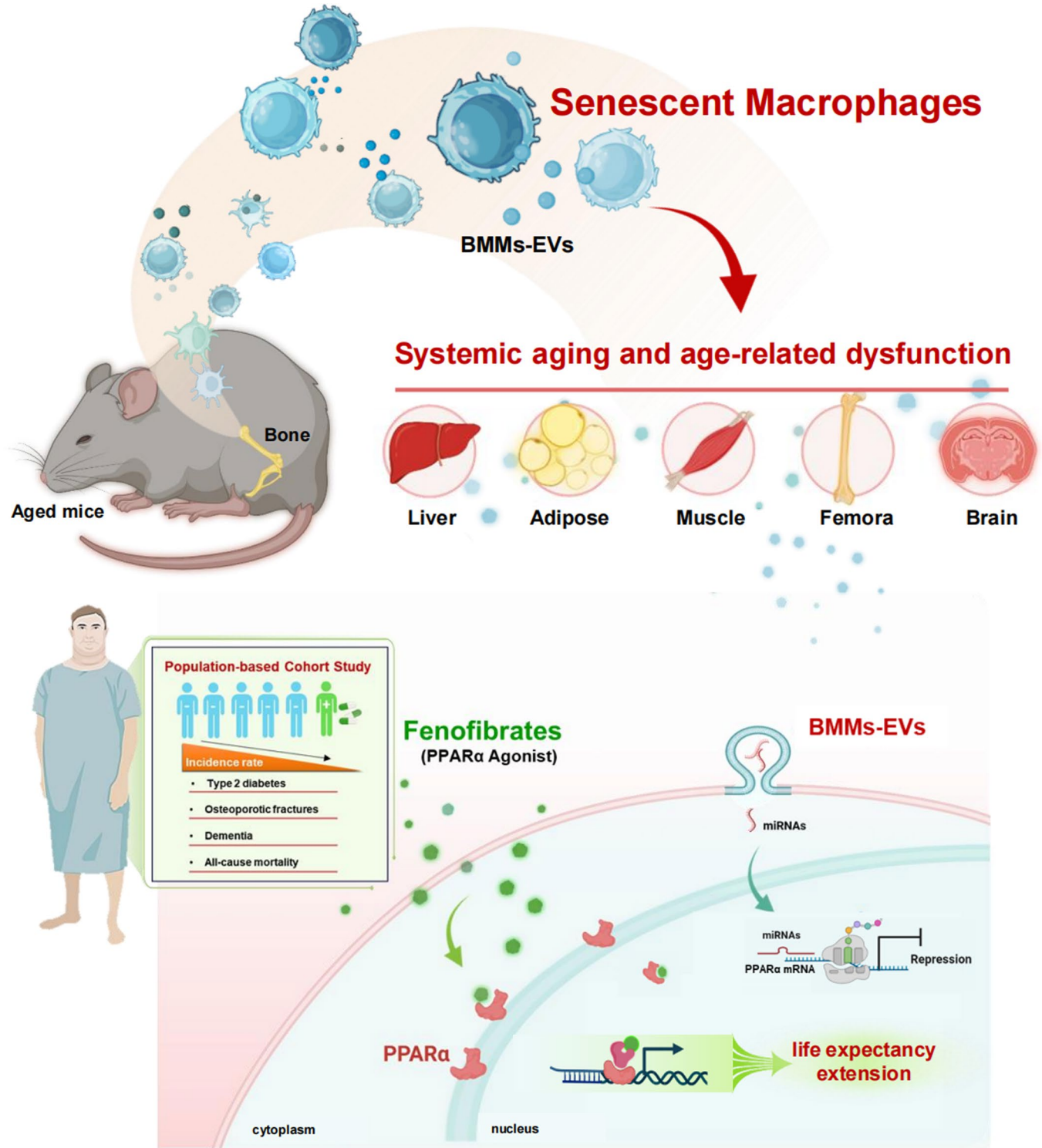

Extended Data Fig. 10 | Schematic representation of key findings. Aged bone marrow macrophages induce paracrine senescence through extracellular vesicles, driving systemic aging and age-related dysfunction through PPARα signalling.

nature portfolio

Corresponding author(s): Chao Zeng, Guang-Hua Lei,Chang-Jun Li

Last updated by author(s): Jing Hou, Kai-Xuan Chen, Chen He, Xiao-Xiao

Reporting Summary

Nature Portfolio wishes to improve the reproducibility of the work that we publish. This form provides structure for consistency and transparency in reporting. For further information on Nature Portfolio policies, see our Editorial Policies and the Editorial Policy Checklist.

Statistics

For all statistical analyses, confirm that the following items are present in the figure legend, table legend, main text, or Methods section.

n/a	Confirmed
☐	☒ The exact sample size (*n*) for each experimental group/condition, given as a discrete number and unit of measurement
☐	☒ A statement on whether measurements were taken from distinct samples or whether the same sample was measured repeatedly
☐	☒ The statistical test(s) used AND whether they are one- or two-sided *Only common tests should be described solely by name; describe more complex techniques in the Methods section.*
☒	☐ A description of all covariates tested
☐	☒ A description of any assumptions or corrections, such as tests of normality and adjustment for multiple comparisons
☐	☒ A full description of the statistical parameters including central tendency (e.g. means) or other basic estimates (e.g. regression coefficient) AND variation (e.g. standard deviation) or associated estimates of uncertainty (e.g. confidence intervals)
☐	☒ For null hypothesis testing, the test statistic (e.g. *F*, *t*, *r*) with confidence intervals, effect sizes, degrees of freedom and *P* value noted *Give P values as exact values whenever suitable.*
☒	☐ For Bayesian analysis, information on the choice of priors and Markov chain Monte Carlo settings
☒	☐ For hierarchical and complex designs, identification of the appropriate level for tests and full reporting of outcomes
☒	☐ Estimates of effect sizes (e.g. Cohen's *d*, Pearson's *r*), indicating how they were calculated

Our web collection on statistics for biologists contains articles on many of the points above.

Software and code

Policy information about availability of computer code

Data collection	All data were collected and analyzed using Excel (Microsoft) and Prism 8 (GraphPad) software. Micro-CT images of femoral bones were obtained by using high-resolution μCT (Skyscan 1172, Bruker MicroCT, Kontich, Belgium), NRecon image reconstruction software (version 1.6), and CTVol 3-dimensional model visualization software (Bruker MicroCT, version 2.0). mRNAs were reverse-transcribed and then amplified using a real-time PCR system (Applied Biosystems). For flow cytometry, stained cells were collected by BD FACS Diva software v9.0 and BD flow cytometry Canto II system. The protein levels were visualized using Image Lab (BioRad,Version 6.1) and ChemiDoc XRS imaging system (BioRad).
Data analysis	For μCT analysis of femoral bones, data analysis software (CT Analyser, version 1.9) were used to analyze the trabecular bone parameters. For flow cytometry analysis, data were analyzed by FlowJo V10 (BD Biosciences).The size and concentration of EVs were analyzed with a Nanoparticle Tracking Analysis. The images of staining and western blot data were quantified using ImageJ 1.52 software.All data were analyzed using Excel (Microsoft) and Prism 8 (GraphPad) software. In bar graphs, data are presented as mean values +/- SEM. Statistical significance ($P<0.05$) was computed using two-tailed Student's t-test, Welch's t-test or one-way ANOVA followed by Tukey's multiple comparisons test.n represents the number of samples used in the experiments.

For manuscripts utilizing custom algorithms or software that are central to the research but not yet described in published literature, software must be made available to editors and reviewers. We strongly encourage code deposition in a community repository (e.g. GitHub). See the Nature Portfolio guidelines for submitting code & software for further information.

Data

Policy information about availability of data

All manuscripts must include a data availability statement. This statement should provide the following information, where applicable:

- Accession codes, unique identifiers, or web links for publicly available datasets
- A description of any restrictions on data availability
- For clinical datasets or third party data, please ensure that the statement adheres to our policy

Raw data of metabolomic analysis have been deposited in the Genome Sequence Archive in the National Genomics Data Center, China National Center for Bioinformation, under accession code OMIX006114. Here is a link: https://ngdc.cncb.ac.cn/omix/releaseList. Raw data of RNA sequencing have been deposited in the Sequence Read Archive (SRA), under accession code SRR28495907~ SRR28495911. Here is a link: https://www.ncbi.nlm.nih.gov/sra.Scientific and ethical approval of human data, and statement are described below. The scientific review committee for the IMRD and the institutional review board at Xiangya Hospital approved this study with a waiver of informed consent (23SRC020, 2018091077). THIN is a registered trademark of Cegedim SA in the United Kingdom and other countries. Reference made to the THIN database is intended to be descriptive of the data asset licensed by IQVIA. This work uses de-identified data provided by patients as a part of their routine primary care. Source data are available with this paper. All other data are available from the corresponding author upon reasonable request.

Research involving human participants, their data, or biological material

Policy information about studies with human participants or human data. See also policy information about sex, gender (identity/presentation), and sexual orientation and race, ethnicity and racism.

Reporting on sex and gender	Men and women.
Reporting on race, ethnicity, or other socially relevant groupings	We used data from IMRD, incorporating data from The Health Improvement Network (THIN), a Cegedim database from general practitioners (GPs) in the UK. IMRD contains anonymized medical records from 839 general practices with approximately 19 million patients.
Population characteristics	The details were listed in Tables of population cohort. We included individuals who were aged 40 to 90 years old, diagnosed with pre-diabetes, and had at least one year of active enrolment with the general practice from January 2000 to December 2022.Pre-diabetes was defined by baseline impaired fasting blood glucose (5.6-6.9 mmol/L), impaired glucose tolerance (glucose tolerance test result 7.8-11.0 mmol/L), HbA1c of 5.7% to 6.4%, or a combination of these results
Recruitment	The details were listed in the METHODS.We used data from IMRD, incorporating data from The Health Improvement Network (THIN), a Cegedim database from general practitioners (GPs) in the UK. IMRD contains anonymized medical records from 839 general practices with approximately 19 million patients. Health care information is recorded at each practice on socio-demographics, anthropometrics, lifestyle factors, visits to GPs, diagnoses from specialists and hospital admissions, and laboratory test results. A previous study has demonstrated the validity of the IMRD database in clinical and epidemiological research
Ethics oversight	The scientific review committee for the IMRD and the institutional review board at Xiangya Hospital approved this study with a waiver of informed consent (23SRC020, 2018091077).

Note that full information on the approval of the study protocol must also be provided in the manuscript.

Field-specific reporting

Please select the one below that is the best fit for your research. If you are not sure, read the appropriate sections before making your selection.

☒ Life sciences ☐ Behavioural & social sciences ☐ Ecological, evolutionary & environmental sciences

For a reference copy of the document with all sections, see nature.com/documents/nr-reporting-summary-flat.pdf

Life sciences study design

All studies must disclose on these points even when the disclosure is negative.

Sample size	No statistical methods were used to predetermine sample size. The sample sizes chosen are consistent with previously published works. Here are references: 1. Li, C.J., et al., Senescent immune cells release grancalcin to promote skeletal aging. Cell Metab, 2021. 33(10): p. 1957-1973.e6. 2. Zou, N.Y., et al., Age-related secretion of grancalcin by macrophages induces skeletal stem/progenitor cell senescence during fracture healing. Bone Res, 2024. 12(1): p. 6
Data exclusions	No data were excluded from the analyses.
Replication	All experiments were performed at at least 3 times, and all attempts at replication were successful.
Randomization	The mice used to 1) treat vehicle or senolytics, 2) to receive young, old, old treated with vehicle or old treated with vehicle or DQ groups, 3) inject senescent or young cells, 4) treat vehicle or fenofibrate were randomly allocated. Further, the mice in evaluation for senescence as well

as aging related tissue phenotypes, aging related gene/protein expression and behavior tests were also randomly assigned. In ex vivo, experiments control and test wells were randomly assigned for each experimental repeat.

Blinding: The investigators were not blinded to allocation during experiments and outcome assessments, but the experiments were performed in appropriate biological replication by independent personal to avoid bias.

Behavioural & social sciences study design

All studies must disclose on these points even when the disclosure is negative.

Study description	n/a.
Research sample	n/a.
Sampling strategy	n/a.
Data collection	n/a.
Timing	n/a.
Data exclusions	n/a.
Non-participation	n/a.
Randomization	n/a.

Ecological, evolutionary & environmental sciences study design

All studies must disclose on these points even when the disclosure is negative.

Study description	n/a.
Research sample	n/a.
Sampling strategy	n/a.
Data collection	n/a.
Timing and spatial scale	n/a.
Data exclusions	n/a.
Reproducibility	n/a.
Randomization	n/a.
Blinding	n/a.

Did the study involve field work? ☐ Yes ☐ No

Field work, collection and transport

Field conditions	n/a.
Location	n/a.
Access & import/export	n/a.
Disturbance	n/a.

Reporting for specific materials, systems and methods

We require information from authors about some types of materials, experimental systems and methods used in many studies. Here, indicate whether each material, system or method listed is relevant to your study. If you are not sure if a list item applies to your research, read the appropriate section before selecting a response.

Materials & experimental systems

n/a	Involved in the study
☐	☒ Antibodies
☐	☒ Eukaryotic cell lines
☒	☐ Palaeontology and archaeology
☐	☒ Animals and other organisms
☐	☒ Clinical data
☒	☐ Dual use research of concern
☒	☐ Plants

Methods

n/a	Involved in the study
☒	☐ ChIP-seq
☐	☒ Flow cytometry
☒	☐ MRI-based neuroimaging

Antibodies

Antibodies used

The detailed information of all antibodies used in the study: Mouse monoclonal anti-p-γH2AX (Santa Cruz, sc-517348, clone: Ser 139, 1:100 dilution); Mouse monoclonal anti-p21 (Santa Cruz, sc-6246, clone: F-5, 1:100 dilution); Mouse monoclonal anti-p53 (Cell signaling Technology, 2524s, clone: 1C12, 1:500 dilution); Rabbit monoclonal anti-p-IR (Cell signaling Technology, 3024s, clone: 19H7, 1:1000 dilution); Rabbit monoclonal anti-IR (Cell signaling Technology, 3025s, clone: 4B8, 1:1000 dilution); Rabbit polyclonal anti-p-AKT (Cell signaling Technology, 9271s, 1:1000 dilution); Rabbit polyclonal anti-AKT (Cell signaling Technology, 9272s, 1:1000 dilution); Rabbit polyclonal anti-p-GSK3β (Cell signaling Technology, 9336s, 1:1000 dilution); Rabbit monoclonal anti-GSK3β (Cell signaling Technology, 9315s, clone: 27C10, 1:1000 dilution); Mouse monoclonal anti-PPARα (Santa Cruz, sc-398394, clone: H-2, 1:100 dilution); Mouse monoclonal anti-PSD95 (Santa Cruz, sc-32290, clone: 7E3, 1:100 dilution); Mouse monoclonal anti-GluR-1 (Santa Cruz, sc-55509, clone: G-12, 1:100 dilution); Rabbit polyclonal anti-IBA1 (Proteintech, 10904-1-AP, 1:100 dilution); Rat monoclonal anti-F4/80 (Abcam, ab6640, clone: CI:A3-1, 1:200 dilution); Mouse monoclonal anti-Osteocalcin (Takara, M188, Clone: R21C-01A, 1:300 dilution); fluorescence-conjugated secondary antibodies Alexa Fluor 488 conjugated anti-rabbit (Invitrogen, A21206, 1:200) or Alexa Fluor 555 conjugated anti-Rabbit (Invitrogen, A21428, 1:200) or Alexa Fluor 555 conjugated anti-mouse (Invitrogen, A31570, 1:200).

Validation

The details validation is listed below. Mouse monoclonal anti-p-γH2AX, RRID: AB_2783871; Mouse monoclonal anti-p21, RRID: AB_628073; Mouse monoclonal anti-p53, RRID: AB_331743; Rabbit monoclonal anti-p-IR, RRID: AB_331253; Rabbit monoclonal anti-IR, RRID: AB_2280448; Rabbit polyclonal anti-p-AKT, RRID: AB_329825; Rabbit polyclonal anti-AKT, RRID: AB_329827; Rabbit polyclonal anti-p-GSK3β, RRID: AB_331405; Rabbit monoclonal anti-GSK3β, RRID: AB_490890; Mouse monoclonal anti-PPARα, RRID: AB_2885073; Mouse monoclonal anti-PSD95, RRID: AB_628114; Mouse monoclonal anti-GluR-1, RRID: AB_629532; Rabbit polyclonal anti-IBA1, RRID:AB_2224377; Rat monoclonal anti-F4/80, RRID:AB_1140040; Mouse monoclonal anti-Osteocalcin, RRID: AB_2935810. Alexa Fluor 488 conjugated anti-rabbit, RRID: AB_2535792; Alexa Fluor 555 conjugated anti-Rabbit, RRID: AB_2535849; Alexa Fluor 555 conjugated anti-mouse, RRID: AB_2536180.

Eukaryotic cell lines

Policy information about cell lines and Sex and Gender in Research

Cell line source(s)

The details were listed in key resources table.These cells were validated by the company.Mouse bone marrow macrophages were isolated as described previously. Briefly, Wild-type male mice were sacrificed, and femurs and tibias were removed and flushed with α-MEM essential medium (Gibco). Bone marrow cells were cultured overnight in α-MEM medium containing 10% fetal bovine serum. Then, we discarded the adherent cells and cultured the floating cells with 30ng/ml M-CSF (Proteintech, HZ-1192)) to obtain monocytes and macrophages. Primary mouse hepatocytes were harvested as previously described. Briefly, male mice were anesthetized with pentobarbital, and the digestive solution was perfused into the inferior vena cava to obtain primary hepatocytes. Primary hepatocytes were cultured in DMEM medium containing 10% fetal bovine serum (Gibco).
Mouse myoblast cell line C2C12 and mouse preadipocyte cell line 3T3-L1 were purchased from the Procell Life Science & Technology Co. Ltd. (Wuhan, China, CL-0006 and CL-0044).

Authentication

Mouse bone marrow macrophages were isolated using standard published protocols and validated by flow analysis. Primary mouse hepatocytes were isolated by using standard published protocols.
The STR profiling authentication procedures of C2C12 and 3T3L1 cells were performed by the Procell Life Science & Technology Co. Ltd. (Wuhan, China)

Mycoplasma contamination

Cells were tested for mycoplasma and all cells tested negative.

Commonly misidentified lines
(See ICLAC register)

No commonly misidentified cell line was used in this study.

Palaeontology and Archaeology

Specimen provenance

n/a.

Specimen deposition	n/a.
Dating methods	n/a.

☐ Tick this box to confirm that the raw and calibrated dates are available in the paper or in Supplementary Information.

Ethics oversight	

Note that full information on the approval of the study protocol must also be provided in the manuscript.

Animals and other research organisms

Policy information about studies involving animals; ARRIVE guidelines recommended for reporting animal research, and Sex and Gender in Research

Laboratory animals	Wild type (WT) male C57BL/6 mice were purchased from SLAC Laboratory Animal Company of Hunan Province and maintained in SPF environment until the age of 16-24 months. For D+Q treatment, sixteen-month-old WT mice were randomly divided into 2 groups and were given Vehicle (PEG 400) or Dasatinib (5 mg/kg, LC labs, D-3307) plus Quercetin (50 mg/kg, Sigma-Aldrich, Q4951) by gavage twice a week for 5months. For fenofibrate treatment, aged WT mice (23m) were given Vehicle or fenofibrate (100 mg/kg/d, Sigma-Aldrich, F6020) by gavage daily for 5 weeks. MiR-378a floxed heterozygous mice were generated by Nanjing GemPharmatech CO., Ltd, and homozygous mice were obtained by crossing.All animal care protocols and experiments were reviewed and approved by the Animal Care and Use Committee of Laboratory Animals Research Center, Xiangya Medical School, Central South University. Mice were kept at 20 to 24°C with a 12-h light/dark cycle, and all mice were provided with food and water ad libitum. Room temperature: 20~26°C; Daily temperature difference: ≤4°C; Relative humidity: 40%~70%.
Wild animals	The study did not involve wild animals.
Reporting on sex	Male.
Field-collected samples	The study did not involve samples collected from the field.
Ethics oversight	All animal care protocols and experiments were reviewed and approved by the Animal Care and Use Committee of Laboratory Animals Research Center, Xiangya Medical School, Central South University, under the active protocol 2019030214.

Note that full information on the approval of the study protocol must also be provided in the manuscript.

Clinical data

Policy information about clinical studies

All manuscripts should comply with the ICMJE guidelines for publication of clinical research and a completed CONSORT checklist must be included with all submissions.

Clinical trial registration	The scientific review committee for the IMRD and the institutional review board at Xiangya Hospital approved this study with a waiver of informed consent (23SRC020, 2018091077).
Study protocol	The details were listed in the METHODS. We included individuals who were aged 40 to 90 years old, diagnosed with pre-diabetes, and had at least one year of active enrolment with the general practice from January 2000 to December 2022. Pre-diabetes was defined by baseline impaired fasting blood glucose (5.6-6.9 mmol/L), impaired glucose tolerance (glucose tolerance test result 7.8-11.0 mmol/L), HbA1c of 5.7% to 6.4%, or a combination of these results. To improve the robustness of observational analysis, we followed the target trial emulation design framework and adopted a prevalent new user design to compare the risk of incident type 2 diabetes between fenofibrate initiators and active comparators (i.e., simvastatin users). We assembled a study cohort including patients initiating therapy with fenofibrate or receiving simvastatin during the study period and then stratified the fenofibrate users into two types: those who switched to fenofibrate (also called prevalent new users) and those who were incident new users. We considered the switching date or date of incident use as the index date. For each prevalent new user, we matched up to five people who continued simvastatin and had used the simvastatin for the same duration at the time of the index date. For each incident new user, we matched up to five incident new users of simvastatin. We excluded patients who were diagnosed with diabetes before the index date. To assess the extra benefits of fenofibrate, we also examined the relation of fenofibrate initiation to the risk of several secondary outcomes, including all-cause mortality, incident major osteoporotic fracture (hip, vertebral, wrist, and humerus fracture), and incident dementia among individuals who were diagnosed with either pre-diabetes or type 2 diabetes.
Data collection	The details were listed in the METHODS. We used data from IMRD, incorporating data from The Health Improvement Network (THIN), a Cegedim database from general practitioners (GPs) in the UK. IMRD contains anonymized medical records from 839 general practices with approximately 19 million patients. Health care information is recorded at each practice on socio-demographics, anthropometrics, lifestyle factors, visits to GPs, diagnoses from specialists and hospital admissions, and laboratory test results. A previous study has demonstrated the validity of the IMRD database in clinical and epidemiological research. The scientific review committee for the IMRD and the institutional review board at Xiangya Hospital approved this study with a waiver of informed consent (23SRC020, 2018091077).
Outcomes	The details were listed in the METHODS. The primary outcome was incident type 2 diabetes. We defined type 2 diabetes using Read codes. This approach has been used in the previous study. The event date is defined by the date of diagnosis. Secondary outcomes included all-cause mortality, incident major osteoporotic fracture (hip, vertebral, wrist, and humerus fracture), and incident dementia. The death date recorded in THIN is linked to the National Health Service; thus, a change in vital status to “dead” is

immediately updated in the individual's electronic health record. Major osteoporotic fracture (hip, vertebral, wrist, and humerus fracture) and dementia were identified by the Read codes, respectively, which have been used in previous studies by using the IMRD database.
Additionally, we estimated life expectancy for patients diagnosed with either pre-diabetes or type 2 diabetes who initiated therapy with fenofibrate or received simvastatin using Abridged period life tables based on the Chiang II method. Life tables were constructed from 2000 to 2022, aggregating death and population data into 5-year age intervals up to 90 years. The difference in life expectancy was calculated as the estimated life expectancy in patients treated with simvastatin minus that in patients treated with fenofibrate.

Dual use research of concern

Policy information about dual use research of concern

Hazards

Could the accidental, deliberate or reckless misuse of agents or technologies generated in the work, or the application of information presented in the manuscript, pose a threat to:

No	Yes	
☒	☐	Public health
☒	☐	National security
☒	☐	Crops and/or livestock
☒	☐	Ecosystems
☒	☐	Any other significant area

Experiments of concern

Does the work involve any of these experiments of concern:

No	Yes	
☒	☐	Demonstrate how to render a vaccine ineffective
☒	☐	Confer resistance to therapeutically useful antibiotics or antiviral agents
☒	☐	Enhance the virulence of a pathogen or render a nonpathogen virulent
☒	☐	Increase transmissibility of a pathogen
☒	☐	Alter the host range of a pathogen
☒	☐	Enable evasion of diagnostic/detection modalities
☒	☐	Enable the weaponization of a biological agent or toxin
☒	☐	Any other potentially harmful combination of experiments and agents

Plants

Seed stocks	n/a.
Novel plant genotypes	n/a.
Authentication	n/a.

ChIP-seq

Data deposition

☐ Confirm that both raw and final processed data have been deposited in a public database such as GEO.

☐ Confirm that you have deposited or provided access to graph files (e.g. BED files) for the called peaks.

Data access links *May remain private before publication.*	n/a.
Files in database submission	n/a.

Genome browser session (e.g. UCSC)	n/a.

Methodology

Replicates	n/a.
Sequencing depth	n/a.
Antibodies	n/a.
Peak calling parameters	n/a.
Data quality	n/a.
Software	n/a.

Flow Cytometry

Plots

Confirm that:

☒ The axis labels state the marker and fluorochrome used (e.g. CD4-FITC).

☒ The axis scales are clearly visible. Include numbers along axes only for bottom left plot of group (a 'group' is an analysis of identical markers).

☒ All plots are contour plots with outliers or pseudocolor plots.

☒ A numerical value for number of cells or percentage (with statistics) is provided.

Methodology

Sample preparation	Mouse blood was taken from the tail vein, and approximately 100 μL of peripheral blood was collected in EDTA tubes. The collected blood was resuspended in 10 times the volume of red blood cell lysis buffer and lysed for 10 minutes.
Instrument	Stained cells were collected by BD FACS Diva software v9.0 and BD flow cytometry Canto II system
Software	Data were analyzed by FlowJo V10 (BD Biosciences)
Cell population abundance	The collected blood was resuspended in 10 times the volume of red blood cell lysis buffer and lysed for 10 minutes. The abundance of the cell population is 10*6.
Gating strategy	First, FSC-A/ FSC-H gating was used to group the cells to evaluate the live or dead status of the cells, and then the gate (CD45.1: FITC, CD45.2: APC) was set according to the group of the target cells. Further analysis of the target cells was performed.

☒ Tick this box to confirm that a figure exemplifying the gating strategy is provided in the Supplementary Information.

Magnetic resonance imaging

Experimental design

Design type	n/a.
Design specifications	n/a.
Behavioral performance measures	n/a.

Acquisition

Imaging type(s)	n/a.
Field strength	n/a.
Sequence & imaging parameters	n/a.
Area of acquisition	n/a.

Diffusion MRI ☐ Used ☐ Not used

Preprocessing

Preprocessing software: n/a.

Normalization: n/a.

Normalization template: n/a.

Noise and artifact removal: n/a.

Volume censoring: n/a.

Statistical modeling & inference

Model type and settings: n/a.

Effect(s) tested: n/a.

Specify type of analysis: ☐ Whole brain ☐ ROI-based ☐ Both

Statistic type for inference: n/a.

(See Eklund et al. 2016)

Correction: n/a.

Models & analysis

n/a	Involved in the study
☐	☐ Functional and/or effective connectivity
☐	☐ Graph analysis
☐	☐ Multivariate modeling or predictive analysis

Functional and/or effective connectivity: n/a.

Graph analysis: n/a.

Multivariate modeling and predictive analysis: n/a.